

Article

Geochronology and petrogenesis of the Cryogenian Sukari granite intrusion, Central Eastern Desert, Egypt: Inferences from whole rock geochemistry, zircon U-Pb-Hf isotopes and trace elements

Aya F. Harhash^{1,*}, Ahmed A. Kamal El Deen², Khalil I. Khali¹, Abdel-Kader M. Moghazi¹

¹ Geology Department, Faculty of Science, Alexandria University, Alexandria, Egypt.

² Sukari Gold Mine Ltd.

* Correspondence Address:

Aya F. Harhash: Geology Department, Faculty of Science, Alexandria University, Alexandria, Egypt, E-mail address: aya.fawzy.harhash@gmail.com.

KEYWORDS: Late Neoproterozoic - Arabian-Nubian Shield – Sukari granite - Zircon U–Pb–Hf isotopes – Geochemistry - Egypt.

Received:

May 08, 2024

Accepted:

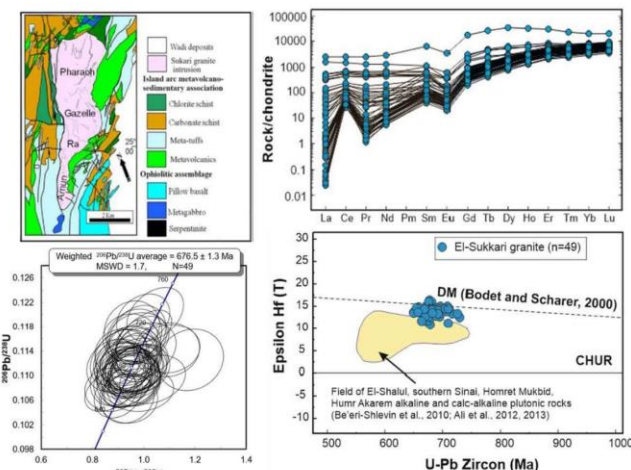
June 08, 2024

Published:

July 06, 2024

ABSTRACT: The Sukari granite intrusion is a trondjemite-granodiorite-granite suite in the Central Eastern Desert (CED) of Egypt. The granites are calc-alkaline and slightly metaluminous to peraluminous (A/CNK molar ratios = 0.91–1.84). On SiO₂ variation diagrams, they exhibit trends of decreasing Al₂O₃, TiO₂, Fe₂O₃^{total}, MgO, CaO, and Sr and increasing Th. The REE patterns are slightly fractionated $\{(La/Yb)_N = 1.89\text{--}2.24\}$ with moderate negative Eu anomalies ($Eu/Eu^* = 0.33 - 0.58$). On primitive-mantle normalized trace element diagram, the granites show negative Nb, Ta, Sr, and Ti anomalies. These geochemical traits suggest that the Sukari granites had evolved by fractional crystallization of plagioclase and ferromagnesian minerals in an island arc tectonic environment. Zircons separated from the Sukari granites are HREE-enriched with positive Ce- and negative Eu- anomalies. The calculated crystallization temperatures of zircons range between 606 and 819°C, which reflect their magmatic origin. Zircon U–Pb–Hf isotope characteristics of the Sukari granite reveal an emplacement age of 676.5 ± 1.3 Ma, positive $\epsilon_{Hf}(t)$ (+10.7 to +16.2), single-stage Hf model age (T_{DM}) of 608–838 Ma, and two-stage Hf model age (T_{DMC}) of 574 - 920 Ma. The absence of zircon inheritance, as indicated by the positive $\epsilon_{Hf}(t)$ and the near crystallization ages $Hf-T_{DM}$, indicates a juvenile protolith for the Sukari granite. According to whole rock geochemistry and isotope signature, the parent magma of the Sukari granite is believed to have been formed by partial melting of a metasomatized mantle source.

Sukari Granite Intrusion, Eastern Desert, Egypt



1. INTRODCTION

The Precambrian rocks of northeast Africa and western Arabia are termed the Arabian Nubian Shield (ANS). The ANS is thought to be a collection of ophiolite relics and volcanic arcs

were amalgamated during the assembly of the supercontinent Gondwana [1].

The crust in the ANS was formed during the Pan-African orogenic event between 850–550 Ma [1–10] through three tectonic stages, namely: Cryogenian pre-collision, collision, and Ediacaran post-collision stages [11–17]. Granitoid rocks are widespread all over the ANS constituting about 40% of the intrusive assemblage [18]. The granitoids were intruded during the pre- and post-collision stages of the shield evolution. The pre-collision granitoids (i.e. syn-tectonic older granites) are subduction-related calc-alkaline quartz diorite-tonalite-trondhjemite-granodiorite suites that were formed during the Cryogenian period between 850 and 650 Ma [1, 19–24]. The post-collision granites (i.e. younger granites) are calc-alkaline, alkaline to peralkaline A2-type granites that were emplaced during the Ediacaran period between 620 and 550 Ma and are thought to be essential in the final consolidation of the ANS [1, 19, 23, 25–26].

The Sukari granite intrusion, which represent the target area of our study, lies in the CED (**Figure. 1a**). It is one of the largest sites of gold production in Egypt with resources of >12 million ounces (Moz) of Au and a reserve of ~5.8 Moz (<https://www.centamin.com/>). Previous geochronological and geochemical investigations show some conflict and have not helped to elucidate its age and tectonic setting [27–32]. The pluton is compositionally heterogeneous and ranges from tonalite-granodiorite to trondhjemite and monzogranite [28, 33–34]. It was interpreted as a Cryogenian syn-tectonic older granite [30–33] or Ediacaran post-collision younger granite [27–29, 35–36]. Its crystallization age was estimated to be 559 ± 6 Ma based on Rb/Sr isotopes and it was affected by Na-metasomatism event at about 520 ± 11 Ma ago [27]. A zircon U-Pb age of 689 ± 3 Ma was determined for the Sukari granite [30] whereas SHRIMP zircon $^{206}\text{Pb}/^{238}\text{U}$ ages of $663\text{--}672$ Ma were obtained [31] for three samples from the Sukari granite. Recently, zircon U-Pb ages for three samples yielded a crystallization age of $\sim 695 \pm 2$ Ma [32]. The zircon ages indicate that the Sukari granite intrusion is of late Cryogenian age and belongs to the older granite group of the basement complex of Egypt. Despite the widespread occurrence of zircons in the Sukari granite and its petrogenetic importance, studies concerning its trace element contents and Lu-Hf isotopic composition have not been carried out so far. In this contribution, we present new whole-rock geochemical data and zircon U-Pb-Hf isotopes and trace elements for the Sukari granite intrusion. The main objective is to provides insights into the age and tectonic and magmatic evolution of this intrusion.

2. Geologic background

The Sukari area is part of the Precambrian basement complex of the CED of Egypt (**Figure. 1a**) and represents the northern extension of the extensive Wadi Ghadir ophiolite sequence [37]. The main rock types in the Sukari area comprise ophiolitic melange rocks, metagabbro, and arc metavolcano-sedimentary assemblage that were intruded by the Sukari granite intrusion [32–33, 38–39]. The ophiolitic rocks consist of dismembered succession of serpentinites followed upward by metagabbro and sheeted dykes [36, 40]. The serpentinites occur as thrust sheets and lenses trending E-W or NW-SE in an island arc metavolcano-sedimentary association in the western and southeastern parts of the area (**Figure. 1b**). The serpentinites

are highly brecciated and fragmented whereby the massive green fragments are surrounded by talc-carbonate indicating and marking shearing along thrust zones [40]. Along the thrust zones, the serpentinites are also listwaenitized with abundant sulphide and oxide minerals. The metagabbro forms lenticular masses ($1\text{--}3 \text{ km}^2$) cutting the serpentinite and overlain by island arc volcaniclastic metasediments [38, 40]. They are weakly metamorphosed and intensely sheared.

The metavolcano-sedimentary rocks form elongate belts trending NE-SW (**Figure. 1b**). They are subdivided into metasedimentary and metavolcanic lava flows and pyroclastics. All represent the product of island arc (770 – 660 Ma) activity [41–42]. The metavolcano-sedimentary rocks are tectonically mixed with the ophiolitic rocks and are intruded by the Sukari granite intrusion. The metavolcanics are mafic to felsic and represented by dark grey to greenish grey metabasalt, meta-andesite and metadacite interlayered with metapyroclastic rocks of meta-lapilli tuffs and meta-agglomerate. The metasedimentary rocks are commonly greenish grey to black and fine-to medium-grained. They are composed mainly of metagreywacke, metamudstone, metasiltstones, in addition to mica- and chlorite schists. The metasediments are highly sheared and cut by many quartz veins along shear zones where silicification and ferrugination are common near the quartz veins.

The Sukari granite (**Figure. 1b**) is a NNE-elongated intrusion dipping $65\text{--}70^\circ\text{E}$. It has sharp contacts against the surrounding country rocks where apophyses and dykes of the granite cut the adjacent rock units. Furthermore, few hornfels occurrences are developed in the country rocks owing to the thermal effect at the time of the granite intrusion at the eastern contact. The contact of the granite with the metavolcano-sedimentary rocks in the western side is a protracted shear zone characterized by occurrence of the main gold-bearing quartz vein in the area. Along the shear zone, the granite exhibits selective and widespread alteration. The contact between the Sukari granite and the metagabbro complex is of tectonic nature. Joints in the granite follow the NNE-SSW, NW-SE and NE-SW trends of which the NE-SW trend is parallel to the mineralized quartz veins and is weakly developed in the eastern part of the granite pluton. The Sukari granite intrusion was subdivided into four geologic domains, namely: Pharaoh, Gazelle, Ra and Amun (**Figure. 1b**). The Pharaoh and Gazelle domains are dominated by conjugate arrays of gentle NE and SW-dipping brittle-ductile shear zones. The thrust kinematic indicators are en-echelon extension and shear extension veins concordant with the shear zones. The style of veining in Ra domain is consistent with Pharaoh and Gazelle zones, but in the Ra domain the shear zones are horizontal and dip moderately SE, indicating SW shortening direction and minimum compression dips steeply to the NW [43]. The Amun domain covers about 0.18 km^2 ($0.9 \text{ km} \times 0.2 \text{ km}$) and lies in the extreme south of the pluton. It is confined to a shallow W-NW dipping shear zone known as the Osiris shear zone.

3. Analytical techniques

Based on microscopic observations, 15 fresh granite samples from the Sukari granite were selected for major and trace element analyses.

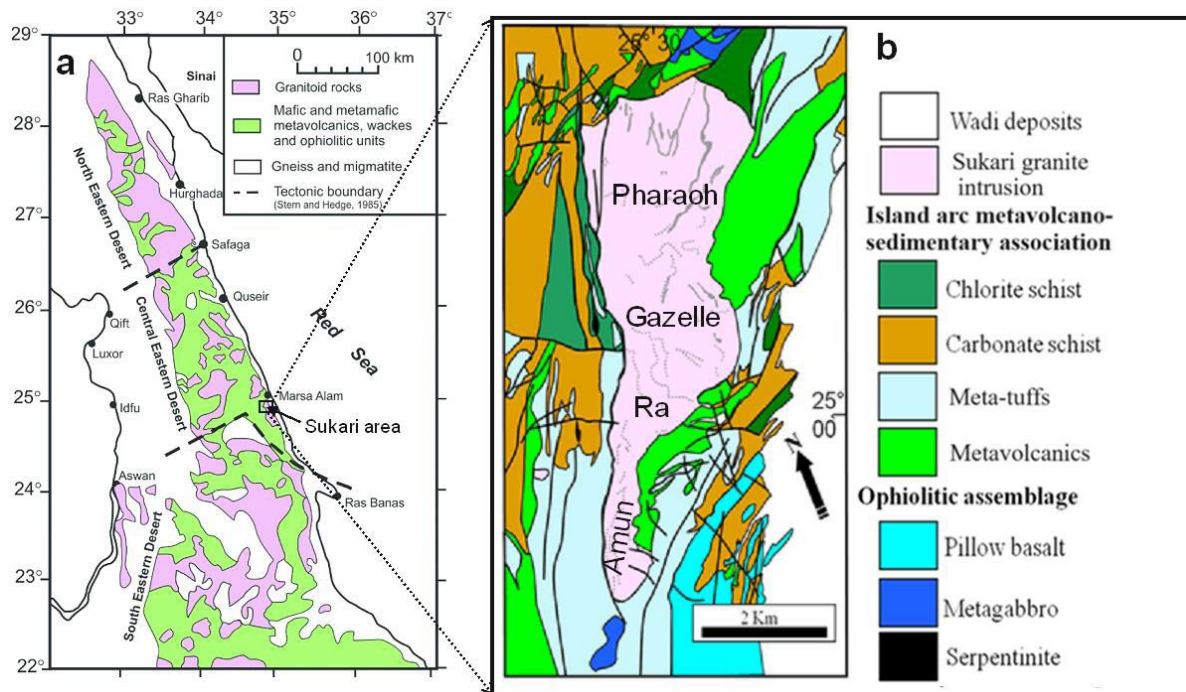


Figure 1. (a) Simplified geologic map of the Eastern Desert of Egypt showing the location of the Sukari area, (b) Geologic map of the Sukari area modified from [43].

Samples were crushed and packed in transparent zip locks, then sorted in a tightly closed plastic container to avoid contamination. Major elements in addition to the trace elements Ba, Sr, Sc, Ni, Nb, Y, and Zr were determined by LiBO₂/Li₂B₄O₇ fusion using inductively coupled plasma-emission spectroscopy (ICP-ES). The rest of trace elements, including the rare earth elements (REEs), were determined using inductively coupled plasma-mass spectroscopy (ICP-MS). The analyses have been carried out at the Acme Analytical Laboratories (ACME LAB), Vancouver, Canada. All major elements are precise within $\pm 1\text{-}5\%$ while trace elements are precise within $\pm 10\text{-}15\%$ as calculated from replicate analyses. The U-Pb-Hf isotopic composition and trace element contents of zircons from sample OS-69 are measured. The zircon grains were separated [44] following the standard procedures at the Pacific Centre for Isotopic and Geochemical Research (PCIGR) laboratory, University of British Columbia, Vancouver, Canada. The procedures include crushing, heavy liquids (Methylene iodide) separation and Frantz isodynamic separator. Inclusion-free zircons were picked for chemical abrasion and leaching. They were analysed for U-Pb isotopes on a Resonetics RESOlution M-50-LR Class I laser ablation system coupled to an Agilent 7700x quadrupole ICP-MS at PCIGR. One spot was measured on 59 zircon grain from the studied sample, along with 53 spot of the 1065 Ma standard 91500 [45], 35 analyses of the Temora2 417 Ma standard [46], and 45 analyses of the 336.9 Ma standard Plešovice [47]. Data were processed using the Isoplot software [48]. The low count rate of ²⁰⁷Pb during analysis may lead to less accurate age of

young (<1.0 Ga) zircons [46]; thus, the ²⁰⁶Pb/²³⁸U ages are considered most reliable and are utilized here.

Hf isotopic composition were determined for the dated zircons of sample OS-69 using a Nu Instruments *Plasma I* multiple collectors inductively coupled plasma mass spectrometry (MC-ICP-MS) at the Pacific Centre for Isotopic and Geochemical Research (PCIGR), University of British Columbia, Vancouver (Canada). Analytical procedures and corrections are described in [49] where the interference of ¹⁷⁶Yb on ¹⁷⁶Lu was treated by correlation of ¹⁷⁶Yb/¹⁷¹Yb and ¹⁷⁴Yb/¹⁷¹Yb replicate analyses of the standards NIST Yb at different concentrations [50]. For Hf isotopes, ¹⁸⁰Ta and ¹⁸⁰W interferences were corrected by analysing ¹⁸¹Ta and ¹⁸³W. Mass bias was corrected by applying ¹⁷⁹Hf/¹⁷⁷Hf = 0.7325 and ¹⁷³Yb/¹⁷¹Yb = 1.1296 [51]. The analyses were performed using different standard zircon references such as GJ-1 ($n = 20$), which yielded an average ¹⁷⁶Hf/¹⁷⁷Hf ratio of 0.282010 ± 0.000081 , 91500- ($n = 20$), which yielded an average ¹⁷⁶Hf/¹⁷⁷Hf ratio of 0.282307 ± 0.000061 , and the Temora-2 ($n=20$), which yielded average ¹⁷⁶Hf/¹⁷⁷Hf = 0.282672 ± 0.000094 . The decay constant used in this study for ¹⁷⁶Lu was $1.867 \times 10\text{-}11\text{yr}^{-1}$ [52]. The initial ¹⁷⁶Hf/¹⁷⁷Hf reported as $\epsilon_{\text{Hf}}(T)$ was calculated using a chondritic reservoir with ¹⁷⁶Hf/¹⁷⁷Hf = 0.282772 and ¹⁷⁶Lu/¹⁷⁷Hf = 0.0332 [53]. Single-stage Hf model ages (Hf_{DM}) were calculated using ¹⁷⁶Lu/¹⁷⁷Hf of zircon relative to a depleted mantle with ¹⁷⁶Hf/¹⁷⁷Hf = 0.28325 and ¹⁷⁶Lu/¹⁷⁷Hf = 0.0384 [54]. The two-stage Hf (crustal) model ages ($\text{T}_{\text{DM}}^{\text{c}}$) were calculated assuming that zircon's continental crust with ¹⁷⁶Lu/¹⁷⁷Hf = 0.015 [55] that was originally derived from a depleted mantle source [56].

4. Petrography

The Sukari granites are grey, white, and occasionally pink. They are geochemically classified (section 4.2) as a trondhjemite-granodioritic-granite suite. Texturally, these granites are porphyritic for trondhjemite and granodiorite to granophytic and equigranular for granite. They are generally composed of variable amounts of plagioclase feldspar, quartz, K-feldspars and minor hornblende and biotite. Accessories are mainly zircon, titanite and opaque.

The Porphyritic granite or the “Sukari porphyry” is grey to white and consists of phenocrysts of about 0.5 x 0.8cm set in a fine-grained matrix. The phenocrysts constitute about 30 - 40% of the rock and consist of medium-grained euhedral to subhedral tabular crystals of twinned plagioclase, anhedral to subhedral quartz, and minor grains of K-feldspar ([Figure. 2a](#)).

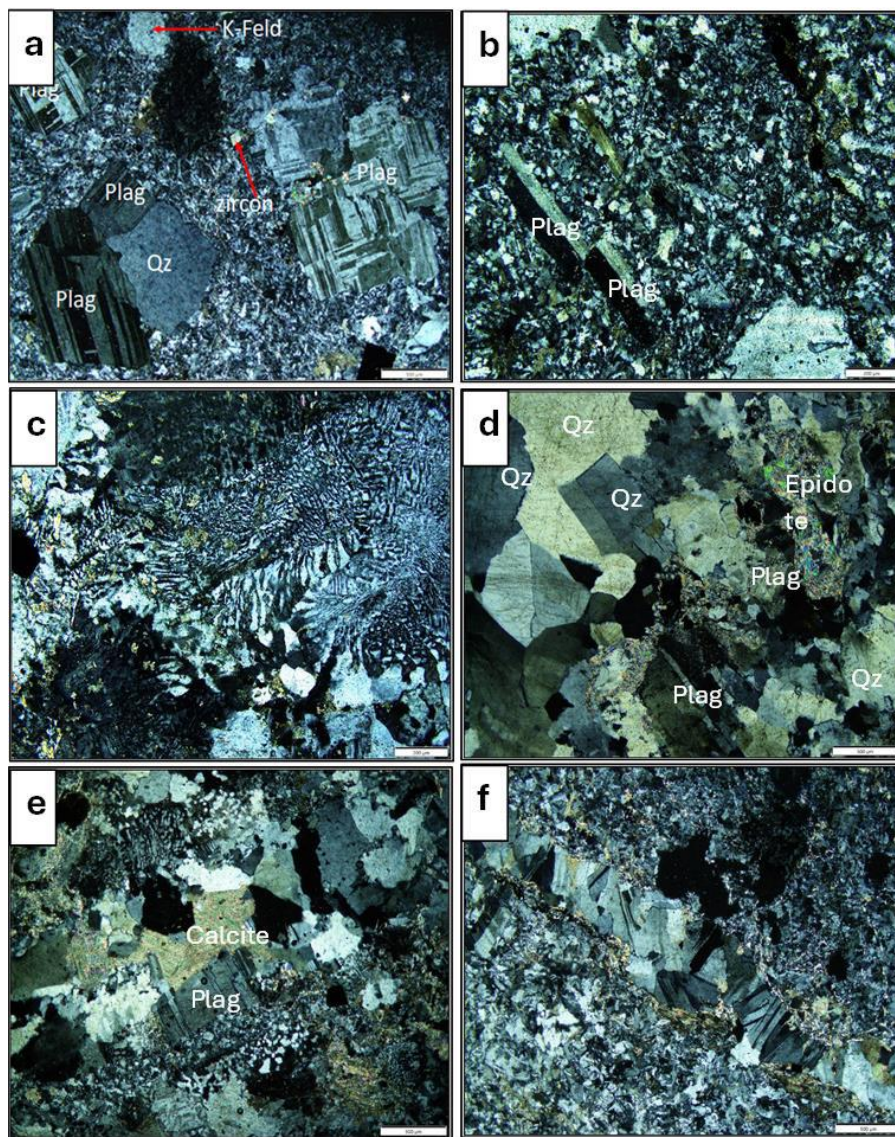


Figure 2. Photomicrographs, in crossed nicols, of the Sukari granite showing: (a) porphyritic texture and mineralogical composition (Plag = plagioclase feldspar, Qz = quartz, K-feld = K-feldspar and zircon) of the Sukari porphyry, (b) fine-grained prismatic phenocrysts of plagioclase in a granular groundmass of the Sukari porphyry, (c) feldspars and quartz granophytic intergrowth in the granophytic granite variety, (d) medium-grained plagioclase, quartz and k-feldspar crystals with sericite and epidote patches, (e) calcite alteration after plagioclase feldspar in the granophytic granite, and (f) secondary albite-quartz vein in the Sukari porphyry (the scale bar is 200 μ m in B and C and 500 μ m in A, D, E and F).

Visual estimate of the overall rock composition is ~50-60% plagioclase, ~30-40% quartz, ~8-10% K-feldspar. The plagioclase crystals are tabular, which occasionally altered to sericite and sometimes contain inclusions of quartz. Some plagioclase phenocrysts are prismatic and set in a granular groundmass of quartz and plagioclase (**Figure. 2b**). Variations in interference colour and intensity of alteration in some plagioclase crystals suggest zoning. Quartz occurs both as subhedral phenocrysts (0.5 - 2 mm in diameter) and as anhedral interstitial grains in the groundmass. The few K-feldspar crystals are totally clouded with sericite and are sometimes associated with quartz forming granophytic intergrowths. Biotite occurs as fine-grained tabular to flaky shreds containing apatite, sphene, and zircon inclusions. The biotite is often associated with strongly pleochroic green hornblende, which is mostly subhedral and twinned. The matrix is composed of quartz and plagioclase in addition to K-feldspar. The crystallization sequence suggests early formation of hornblende and biotite followed by plagioclase, quartz, and K-feldspar of variable sizes.

The granophytic granite is light grey and medium- to fine-grained. Generally, this granite variety is characterized by intergrowth textures, where feldspars and quartz intergrown simultaneously forming the characteristic graphic and granophytic textures. Accessories are zircon, apatite, titanite and opaques whereas sericite and calcite are secondary minerals. Plagioclase feldspar is the most abundant mineral constituent. It is euhedral to subhedral tabular crystals and shows albite-Carlsbad twinning and crystallized in association with K-feldspar and quartz. Worm-like blebs of quartz are attached to the rims of the K-feldspar crystals showing explicit graphic and granophytic intergrowths (**Figure. 2c**). Hornblende and biotite are minor phases and are slightly altered to chlorite.

The equigranular granite is characteristically pink and consists mainly of quartz, plagioclase, and orthoclase (**Figure. 2d**) in addition to minor biotite. Sericite, chlorite, calcite and occasionally epidote represent the secondary minerals whereas zircon, apatite, titanite and opaques are accessory minerals. Quartz is the most abundant constituent mineral occurring as anhedral medium-grained crystals, which are occasionally strained and show wavy extinction. Plagioclase also occurs as tabular medium-grained twinned crystals that show evidence of deformation represented by kinking in the twin lamellae. K-feldspar is represented by orthoclase in the form of medium-grained subhedral to anhedral crystals.

Most of the granitic rocks of the Sukari intrusion experienced wide carbonate-sericite alterations, which occurs as replacement for the plagioclase feldspar crystals (**Figure. 2e**) or as a fracture-filling. The altered granites are often cut by fresh albite as secondary albite veins (**Figure. 2f**).

5. Results

5.1. Whole rock major and trace elements

Chemical analyses for the 15 fresh granitic samples from the Sukari pluton are shown in **Table 1**. The analysed samples show some variation in their major and trace element contents such as SiO_2 (68.92 – 75.96 wt.%), Al_2O_3 (10.90 – 13.85 wt.%), TiO_2 (0.15 – 0.30 wt.%), total Fe as Fe_2O_3 (2.91–4.56 wt.%), CaO (0.09 – 1.47 wt.%), MgO (0.04 – 0.81 wt.%),

Na_2O (2.10 – 5.98 wt.%), K_2O (0.47 – 3.28 wt.%), P_2O_5 (0.01 – 0.06 wt.%), Ba (53 – 478 ppm), Rb (10 – 69 ppm), Sr (17 – 72 ppm), Ga (21 – 31 ppm), Hf (14–21 ppm), Nb (16.4 – 23.4 ppm), Ta (1 – 1.7 ppm), Zr (531 – 792 ppm), Y (89 – 138 ppm), U (1.8 – 3.1 ppm), Th (5.1 – 8.2 ppm) and ΣREE (234 – 361 ppm). Using the Q`– ANOR binary classification diagram [57], the Sukari granite samples straddle the granodiorite, monzogranite, syenogranite and alkali-feldspar granite fields (**Figure. 3a**). On the other hand, the Sukari granites are classified as trondhjemite and granite (**Figure. 3b**) on the normative An-Ab-Or ternary classification diagram [58]. On the SiO_2 vs. major and trace element variation diagrams (**Figure. 4**), the contents of Al_2O_3 , TiO_2 , $\text{Fe}_2\text{O}_3^{\text{total}}$, CaO , MgO , and Sr decrease with increasing SiO_2 . On the other hand, Th shows a trend of increasing its contents with increasing SiO_2 whereas Ba data show some scatter.

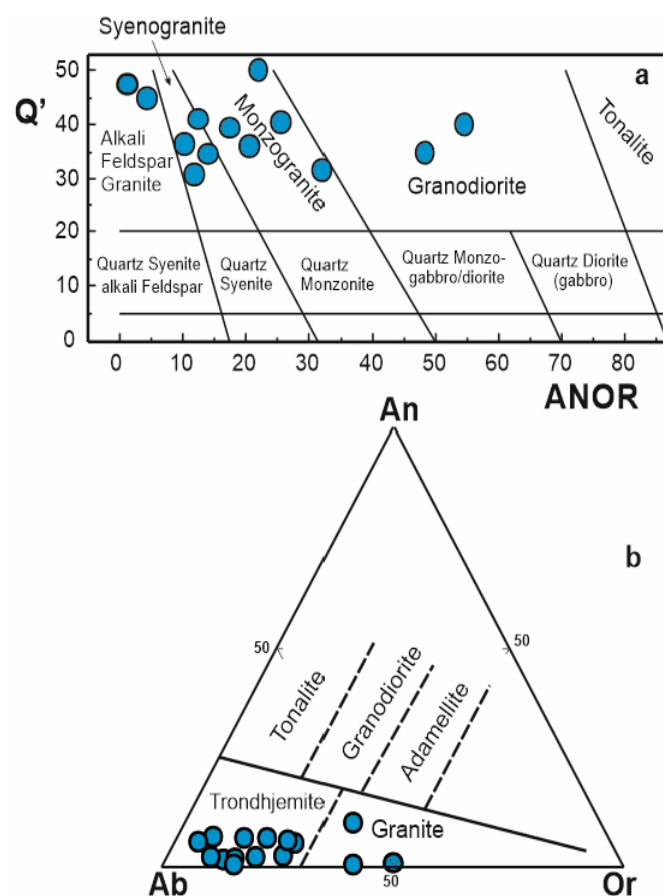


Figure 3. (a) Q`– ANOR classification diagram [57] for the Sukari granites, Q' and ANOR are calculated using norm values where: $Q'=100Q/(Q+\text{Or}+\text{Ab}+\text{An})$ and $\text{ANOR}=100\text{An}/(\text{An}+\text{Or})$, (b) An-Ab-Or normative ternary classification diagram [58] for the Sukari granites.

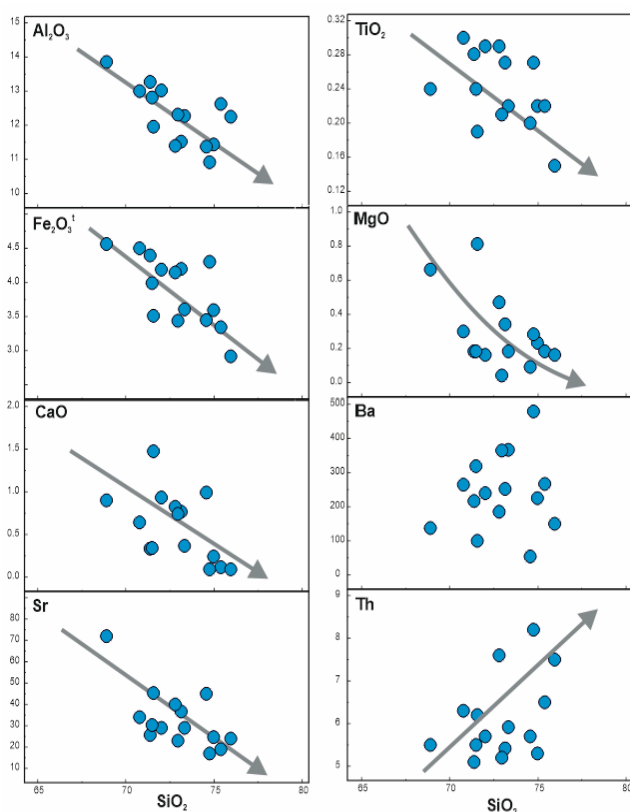


Figure 4. Variation diagrams (SiO₂ vs. some major and trace elements) for the Sukari granite intrusion. Arrows are visual estimate of the evolutionary trends.

The primordial mantle-normalized diagram [59] of (**Figure. 5a**) demonstrates the enrichment and depletion of some trace elements and their systematic variations in the Sukari granite samples. Despite the presence of some inconsistencies in the enrichment and/or depletion of elements, the Sukari granite samples are collectively enriched in LILEs (K, Rb, Ba, Cs, Th, and U) relative to HFSEs (Nb, Ta, Hf, Zr, and Y). All samples have LILE/HFSE ratios >1 and significant Nb-Ta, Sr, and Ti negative anomalies (**Figure. 5a**). Such chemical features, especially the negative Nb-Ta anomalies, characterize subduction-related granites [60-61] or magmas derived by partial melting of a mantle-derived crustal source [62]. The negative anomalies of Ba, Sr, and Ti, on the other hand, emphasize the role of fractionation of the feldspars and the ferromagnesian minerals during the evolution of these rocks. The chondrite-normalized REE patterns of the Sukari granites are given in (**Figure. 5b**). The samples have high REE contents (Σ REEs = 234–361 ppm), chondritic abundance for most elements >50x, LREE-enrichment relative to the HREE { $(La/Yb)_N$ = 1.89–2.24}, weakly fractionated LREE { $(La/Sm)_N$ = 1.53–1.77}, weakly fractionated HREE { $(Gd/Yb)_N$ = 1.01 – 1.23} and moderate negative Eu anomalies (Eu/Eu^* = 0.33 – 0.58).

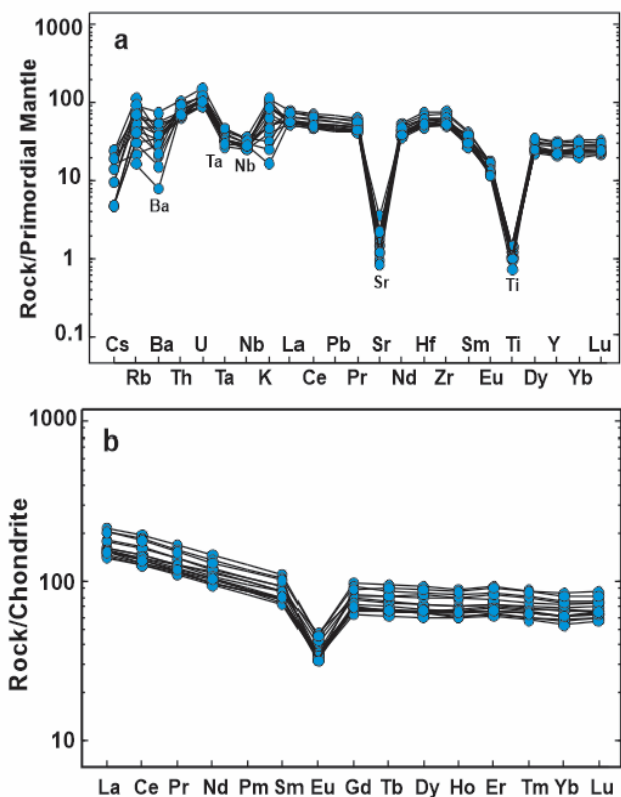


Figure 5. (a) Primitive mantle-normalized multi-element diagrams for the Sukari granites, b) Chondrite-normalized REE patterns of the Sukari granites, normalizing values are from [59].

The Sukari granite have A/CNK molar ratios range from 0.91 to 1.83 and exhibit metaluminous to peraluminous characteristics on the A/CNK vs A/NK binary diagram (**Figure. 6a**) [63-64]. The alkalinity or magma type of the Sukari granites, expressed by the agpaitic index [AI = (Na + K)/Al], is shown as a function of SiO₂ in (**Figure. 6b**) where the Sukari granites show calc-alkaline affinity (AI <0.87). Following the SiO₂ vs modified alkali lime index (MALI = Na₂O + K₂O - CaO) classification [65], the Sukari granite plot mainly in the alkali-calcic and calc-alkalic fields (**Figure. 6c**). It has been documented that the trace element composition correlates to a considerable extent with tectonic setting of granitic rocks [66-68]. The elements Rb, Hf and Ta have long been used to determine the tectonic setting of granitoid rocks [66, 69]. (**Figure. 7d**) shows the Rb-Hf-Ta tectonic discrimination diagram [69] where the Sukari granite samples plot in the field of volcanic arc granite (VAG), which is the field of I-type granites [68].

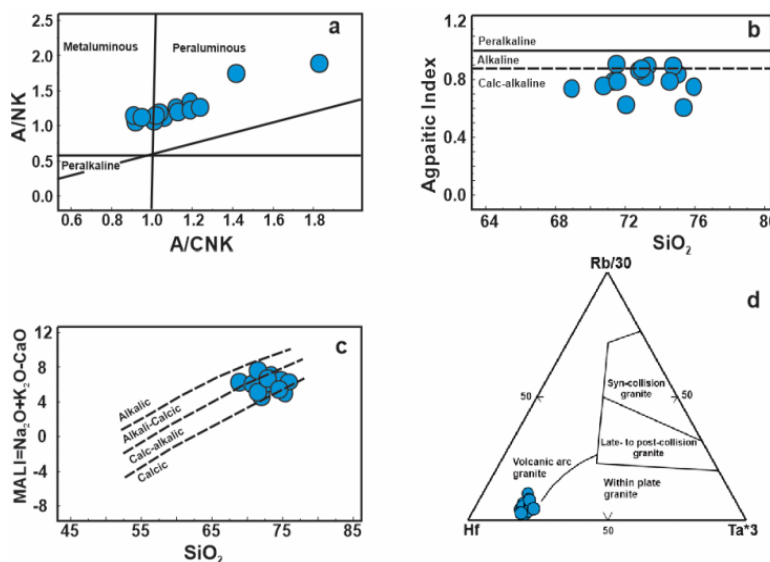


Figure 6. Discrimination diagrams for the Sukari granites: (a) Molar A/NK vs. molar A/CNK diagram of [63] showing the metaluminous to peraluminous compositions, the Shand's indices A/CNK and A/NK are calculated as follows: A/CNK = {molar ratio $\text{Al}_2\text{O}_3/(\text{CaO} + \text{Na}_2\text{O} + \text{K}_2\text{O})$ } and A/NK = {molar ratio $\text{Al}_2\text{O}_3 / (\text{Na}_2\text{O} + \text{K}_2\text{O})$ }; (b) Agpaitic index (AI = Na + K/Al) vs. SiO_2 diagram showing the calc-alkaline character of the Sukari granite, the dashed line with AI = 0.87 and separates alkaline and calc-alkaline granite series; (c) SiO_2 versus modified alkali lime index (MALI = $\text{Na}_2\text{O} + \text{K}_2\text{O} - \text{CaO}$) after [65] showing the calc-alkalic nature of the Sukari granite; (d) Rb/30 – Hf – 3*Ta discrimination diagram [69] for the studied granite intrusions.

Table 1: Whole-rock chemical analyses of major oxides (wt%) and trace elements (ppm) for representative samples of the Sukari granite.

	OS-12	OS-15	OS-24	OS-30	OS-34	OS-35	OS-36	OS-37	OS-43	OS-46	OS-49	OS-53	OS-61	OS-69	OS-70
SiO ₂	75.01	73.35	75.39	68.92	72.04	71.39	70.78	71.52	74.77	73.17	72.81	71.58	72.98	75.96	74.59
TiO ₂	0.22	0.22	0.22	0.24	0.29	0.28	0.3	0.24	0.27	0.27	0.29	0.19	0.21	0.15	0.2
Al ₂ O ₃	11.43	12.26	12.61	13.85	13.01	13.26	12.98	12.8	10.9	11.51	11.38	11.94	12.31	12.23	11.37
Fe ₂ O ₃	3.59	3.6	3.34	4.56	4.18	4.39	4.5	3.98	4.3	4.19	4.14	3.51	3.43	2.91	3.44
MnO	0.06	0.07	0.06	0.02	0.08	0.1	0.09	0.08	0.04	0.05	0.07	0.07	0.08	0.04	0.05
MgO	0.23	0.18	0.18	0.66	0.16	0.18	0.3	0.18	0.28	0.34	0.47	0.81	0.04	0.16	0.09
CaO	0.24	0.36	0.11	0.9	0.93	0.33	0.64	0.34	0.09	0.76	0.82	1.47	0.74	0.09	0.99
Na ₂ O	5.54	5.03	2.1	5.63	2.78	5.79	4.35	5.95	3.29	4.73	5.98	5.86	4.94	5.05	5.86
K ₂ O	1.14	2.47	2.98	1.48	2.67	1.47	2.36	2.05	3.28	1.79	0.93	0.74	2.44	1.32	0.47
P ₂ O ₅	0.04	0.03	0.03	0.06	0.03	0.04	0.04	0.02	0.04	0.03	0.03	0.01	<0.01	0.02	0.02
LOI	2.3	2.2	2.8	3.5	3.7	2.6	3.4	2.6	2.5	3	2.9	3.7	2.7	1.9	2.8
SUM	99.8	99.77	99.82	99.87	99.83	99.74	99.76	99.76	99.84	99.82	99.88	99.87	99.83	99.88	
Sc	2	3	3	4	3	4	4	4	3	3	2	3	<1	3	
Co	0.5	0.6	<0.2	0.6	0.9	0.6	0.9	0.4	0.2	1.6	0.8	0.9	0.3	1.1	0.5
V	<8	<8	<8	14	<8	<8	<8	<8	16	<8	<8	<8	<8	<8	<8
Cr	<14	14	<14	<14	<14	<14	14	<14	<14	<14	<14	<14	<14	<14	<14
Ni	<20	<20	<20	<20	<20	<20	<20	<20	<20	<20	<20	<20	<20	<20	<20
Cs	0.1	0.2	0.5	0.5	0.4	0.1	0.2	0.1	0.3	<0.1	<0.1	0.1	0.3	0.4	<0.1
Ba	225	365	266	137	238	215	263	317	478	251	184	100	363	150	53
Rb	19	38	69	40	49	27	44	28	55	32	13	18	42	25	10
Sr	24.5	28.8	19	71.8	28.7	25.5	33.9	30.3	16.9	36.6	39.8	45.2	23	24	44.7
Be	1	3	3	6	5	4	1	<1	<1	<1	<1	<1	<1	<1	4
Ga	21	24	31	22	28	29	30	23	27	25	24	27	25	28	21
Hf	14	16	17	15	15	16	17	14	21	14	20	17	15	18	15
Ta	1	1.2	1.3	1.2	1.2	1.2	1.4	1.2	1.7	1.2	1.6	1.5	1.2	1.7	1.1
Nb	17	18	17	17	19	19	20	18	23	16	23	20	19	22	19
Zr	531	642	661	589	603	659	658	565	792	542	747	658	570	585	539
Y	93	97	104	99	106	105	118	93	138	89	125	120	97	129	95
Th	5.3	5.9	6.5	5.5	5.7	5.1	6.3	5.5	8.2	5.4	7.6	6.2	5.2	7.5	5.7
U	1.8	2.2	2.6	2.2	1.9	1.9	2.3	1.9	3.1	1.8	2.4	2.3	2.2	2.5	2.1
Sn	5	6	10	6	2	2	10	4	19	10	5	3	6	9	2
W	6.2	7.7	5.6	9	1	5.1	74.2	180.7	9.3	16.6	6.1	1.6	2.9	1.2	3.7
La	34.7	36.1	36.2	37.9	38.3	38.3	42.8	33.8	51.5	33.6	48.1	42.3	36.9	47.9	36.4
Ce	80.3	83.1	80.8	87.1	89.8	90.1	101	78.8	119.7	77.2	112.9	99.6	87.2	110.2	83.6
Pr	10.95	10.97	10.9	11.47	12.18	12.18	13.23	10.75	15.92	10.41	14.98	13.11	11.88	14.51	11.24
Nd	47.2	46.1	45.7	48.2	54.5	52.6	56.9	46.2	68	44	63.8	55.8	50.4	61	48.3
Sm	12.1	11.2	11.76	11.6	13.28	13.44	14.26	11.64	16.97	11.05	15.87	14.22	13.04	15.64	12.25
Eu	2.05	1.94	1.91	2.05	2.36	2.75	2.48	2.02	2.63	1.91	2.62	2.06	1.98	1.83	1.82
Gd	13.9	13.49	14.13	13.9	15.95	15.63	17.04	13.65	20.14	12.72	19.19	16.66	14.87	18.21	14.26
Tb	2.43	2.44	2.52	2.41	2.81	2.75	3.02	2.39	3.51	2.26	3.28	3.05	2.6	3.37	2.46
Dy	16.17	16.02	16.73	16.01	18.03	17.91	20.04	15.94	23.31	15.09	21.53	20.84	17.08	22.81	16.74
Ho	3.45	3.6	3.76	3.56	3.92	3.91	4.41	3.34	5.01	3.39	4.68	4.47	3.72	4.89	3.63
Er	10.34	10.91	11.59	10.9	12.02	11.76	12.68	10.52	15.42	10.03	13.99	13.76	11.24	14.97	10.88
Tm	1.49	1.61	1.72	1.61	1.73	1.76	1.88	1.51	2.24	1.45	2.05	2.01	1.63	2.2	1.62
Yb	9.6	10.35	11.29	10.39	11.23	11.6	12.14	9.82	14.22	8.96	12.65	12.48	10.4	13.88	10.26
Lu	1.48	1.57	1.66	1.59	1.66	1.75	1.86	1.5	2.19	1.44	1.9	1.87	1.57	2.05	1.62

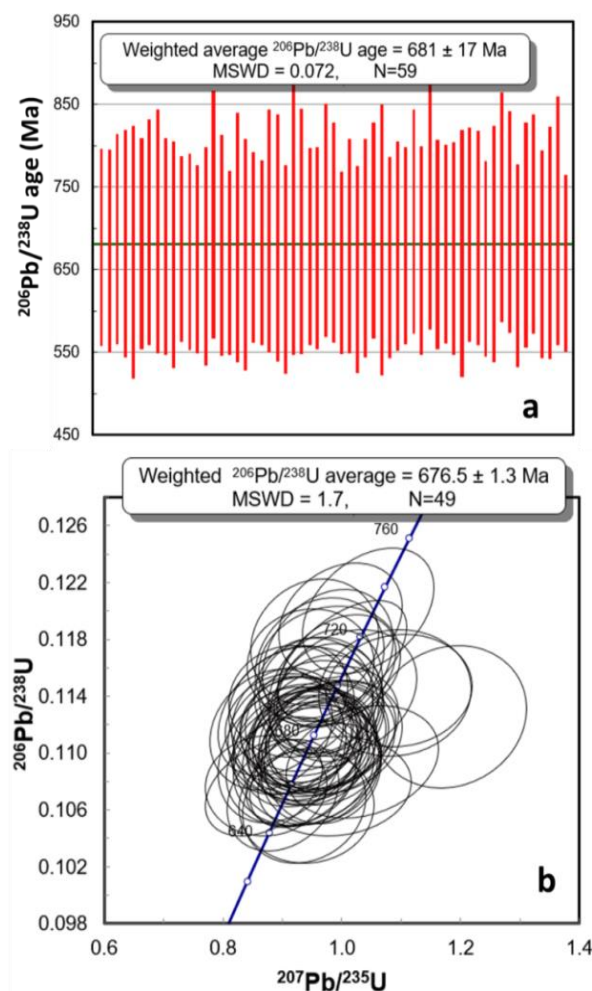


Figure 7. Zircon U-Pb LA-ICP-MS data of sample OS-69 from the Sukari granite intrusion: a) U-Pb weighted mean age, b) U-Pb Concordia diagram.

5.2. Zircon U-Pb geochronology

Zircons extracted from sample OS-69 are mostly inclusion-free, pale brown in colour, subhedral to euhedral and prismatic. They range in size from 250 to 50 μm with length/width ratios between 1.0 and 5.0. The Th and U contents in zircons vary from 81.76 - 253.87 ppm and 35.02 - 172.49 ppm, respectively. The Zircon grains morphologies along with their Th/U ratios between 0.33 and 0.99 (Table 2) support its magmatic origin [70-72]. The calculated age based on the $^{206}\text{Pb}/^{238}\text{U}$ weighted mean values (Table 2) is preferred over the $^{207}\text{Pb}/^{206}\text{Pb}$ age for young zircon grains [73-74] and can be interpreted as the crystallization age. Weighted mean age calculations and Concordia diagrams were plotted using Isoplot software [48]; uncertainties include measured errors and are quoted at the 2σ confidence level. Weighted mean age plot of the 59 analyses give a $^{206}\text{Pb}/^{238}\text{U}$ age of 681 ± 17 Ma (MSWD=0.072) as shown in (Figure. 3a). The data are presented on a Concordia diagram (Figure. 3b) and yielded an age of 676.5 ± 1.3 Ma (n=49 and MSWD=1.7), which is more or less similar to the weighted

average and is taken to be the Sukari granite crystallization age. This age is a little bit younger than the zircon U-Pb ages of 689 ± 2.5 Ma and $\sim 695 \pm 2$ Ma determined by [30, 32], respectively and is similar to a zircon SHRIMP $^{206}\text{Pb}/^{238}\text{U}$ age of 663–672 Ma determined by [31] for the Sukari granite. However, all the obtained ages indicate that this granite intrusion belongs to the Cryogenian older granite group of the Egyptian basement complex.

5.3. Zircon Lu-Hf isotopes

The Lu-Hf isotopic data of zircons of sample OS-69 from the Sukari granite are listed in (Tables 3). The data were processed in a Microsoft Excel spreadsheet to calculate the corrected $^{176}\text{Hf}/^{177}\text{Hf}$ and $^{176}\text{Lu}/^{177}\text{Hf}$ ratios, initial $^{176}\text{Hf}/^{177}\text{Hf}$ reported as $\epsilon_{\text{Hf}}(\text{T})$, single-stage Hf model ages (HfT_{DM}), and two-stage Hf (crustal) model ages ($\text{HfT}_{\text{DM}}^{\text{c}}$) for each of the analysed grains. The zircon grains give $^{176}\text{Hf}/^{177}\text{Hf}$ of 0.282613–0.283041 (average = 0.282796 ± 0.000051). The $\epsilon_{\text{Hf}}(\text{T})$ values are calculated using the 676.5 Ma age of the granite and are used in the $\epsilon_{\text{Hf}}(\text{T})$ – age plot (Figure. 8). Zircons show positive $\epsilon_{\text{Hf}}(\text{T})$ varying from +10.7 to +16.2 (Table 3 and Figure. 8) (weighted mean $\epsilon_{\text{Hf}}(\text{T})$ of 13.7 ± 2) and yielded a single-stage Hf model age (HfT_{DM}) of 608–838 Ma (average 714 Ma) and a two-stage Hf model age ($\text{HfT}_{\text{DM}}^{\text{c}}$) of 574 - 920 Ma (average 732 Ma) (Table 3). The zircon grains show a very narrow range of $\epsilon_{\text{Hf}}(\text{T})$, which is similar to those expected from depleted mantle (Figure. 8). The present Lu-Hf results for the Sukari granites are consistent with other studies on granites from different localities in Egypt, such as: El-Shalul granitic dome in the CED { $(\epsilon_{\text{Hf}}\text{T} = +6.1$ to $+12)$ } [75], Humr Akarim and Humrat Mukbid granites in the SED { $(\epsilon_{\text{Hf}}\text{T} = +11.9$ and $+4$)} [76], and Sinai granites { $\epsilon_{\text{Hf}}\text{T} = +5.5$ to $+13.9$ } [25]. These results support the idea that the Sukari granite magma was derived from a depleted source.

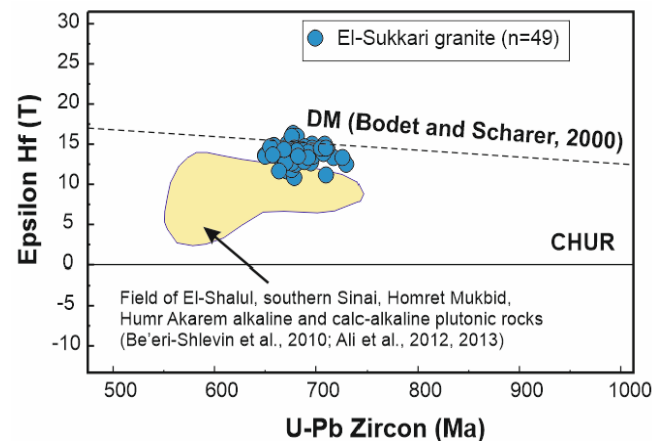


Figure 8. Epsilon $\text{Hf}(\text{T})$ versus U-Pb age plot for zircons from the Sukari granite intrusion, South Eastern Desert of Egypt. DM is the depleted mantle growth curve and CHUR is chondritic uniform reservoir. The field of alkaline and calc-alkaline plutonic rocks for the El-Shalul (CED), southern Sinai, and Homret Mukbid and Humr Akarem (SED) is from [75-76, 131].

Table 2: LA-ICP-MS zircon U-Pb age data for sample OS-69 from the Sukari granite intrusion; the concentrations of U and Th are in ppm.

Grain	U	Th	Th/U	Isotopic Ratios				Isotopic Ages (Ma)							
				$^{207}\text{Pb}/^{235}\text{U}$	$\pm 2\sigma$	$^{206}\text{Pb}/^{238}\text{U}$	$\pm 2\sigma$	$^{207}\text{Pb}/^{206}\text{Pb}$	$\pm 2\sigma$	$^{207}\text{Pb}/^{235}\text{U}$	2σ	$^{206}\text{Pb}/^{238}\text{U}$	2σ	$^{207}\text{Pb}/^{206}\text{Pb}$	2σ
1-1	159.39	81.41	0.51	0.952	0.088	0.1109	0.0030	0.0634	0.0045	674.5	44.6	677.8	17.5	667.1	140.3
1-2	183.18	70.54	0.39	0.944	0.083	0.1101	0.0031	0.0614	0.0036	671.4	42.7	673.5	18.2	641.1	135.0
1-3	143.10	141.12	0.99	0.946	0.088	0.1126	0.0032	0.0609	0.0045	671.0	46.5	688.0	18.4	557.6	178.1
1-5	152.31	72.13	0.47	0.881	0.085	0.1117	0.0035	0.0577	0.0046	636.6	45.3	682.3	20.1	431.0	185.4
1-6	128.15	53.81	0.42	0.899	0.088	0.1099	0.0039	0.0589	0.0043	646.0	47.2	671.9	22.7	488.7	174.6
1-7	152.65	66.15	0.43	0.911	0.088	0.1116	0.0032	0.0589	0.0045	652.5	47.5	682.2	18.6	481.1	185.1
1-8	145.26	58.60	0.40	0.964	0.085	0.1141	0.0034	0.0616	0.0040	681.8	43.6	696.2	19.5	605.9	141.2
1-9	114.70	51.77	0.45	1.007	0.098	0.1142	0.0036	0.0640	0.0045	701.5	48.6	697.1	21.1	676.8	161.3
1-10	148.21	61.69	0.42	0.970	0.097	0.1111	0.0033	0.0634	0.0050	682.2	50.8	678.8	19.3	637.2	187.4
2-1	154.81	69.55	0.45	0.968	0.081	0.1093	0.0035	0.0644	0.0038	684.5	42.7	668.7	20.5	746.1	113.8
2-2	182.52	111.33	0.61	0.921	0.087	0.1106	0.0028	0.0606	0.0046	658.2	45.7	675.9	16.6	549.7	169.7
2-3	211.82	152.38	0.72	0.932	0.080	0.1099	0.0030	0.0616	0.0040	665.4	41.8	672.3	17.5	607.8	141.3
2-4	153.00	69.39	0.45	0.953	0.093	0.1085	0.0029	0.0640	0.0052	674.0	48.3	663.7	17.2	652.3	185.4
2-5	132.39	65.08	0.49	0.936	0.096	0.1091	0.0034	0.0621	0.0050	663.8	51.4	667.1	19.8	587.0	190.3
2-7	145.56	63.81	0.44	0.954	0.088	0.1178	0.0036	0.0586	0.0039	675.4	46.5	717.8	20.8	483.8	169.3
2-9	81.76	37.75	0.46	0.906	0.079	0.1113	0.0034	0.0588	0.0037	651.3	42.3	679.9	19.6	549.3	163.9
2-10	143.18	56.87	0.40	0.873	0.083	0.1077	0.0029	0.0585	0.0043	632.2	46.6	659.3	16.9	467.9	187.5
3-1	100.47	43.35	0.43	0.901	0.089	0.1130	0.0038	0.0574	0.0041	646.8	48.1	689.7	21.8	437.0	169.4
3-2	127.75	55.09	0.43	0.963	0.081	0.1094	0.0036	0.0638	0.0040	681.7	42.2	669.1	20.8	723.4	120.2
3-4	155.00	63.03	0.41	0.952	0.075	0.1109	0.0029	0.0618	0.0030	683.4	43.6	678.0	16.9	665.2	115.3
3-5	151.69	77.39	0.51	0.963	0.084	0.1098	0.0028	0.0632	0.0040	681.0	43.4	671.8	16.6	664.0	137.5
3-7	106.29	35.02	0.33	1.090	0.105	0.1142	0.0036	0.0671	0.0045	742.3	50.2	697.1	21.0	826.5	155.8
3-8	88.23	35.22	0.40	0.936	0.103	0.1129	0.0037	0.0600	0.0057	663.1	52.6	689.6	21.6	489.4	210.0
4-1	127.70	57.92	0.45	0.936	0.085	0.1063	0.0033	0.0634	0.0042	675.8	39.9	651.1	19.3	711.6	135.6
4-2	118.43	57.62	0.49	0.977	0.090	0.1167	0.0040	0.0602	0.0039	687.5	45.5	711.3	22.9	560.7	136.6
4-3	143.79	62.04	0.43	0.971	0.079	0.1142	0.0037	0.0613	0.0032	686.5	41.1	697.0	21.2	645.0	99.4
4-4	141.68	63.66	0.45	0.973	0.083	0.1111	0.0030	0.0632	0.0039	686.8	42.1	679.2	17.5	701.5	116.8
4-5	185.44	89.18	0.48	0.946	0.079	0.1107	0.0031	0.0615	0.0034	673.0	41.7	677.0	17.9	654.4	103.3
4-7	146.79	54.90	0.37	1.000	0.089	0.1166	0.0034	0.0615	0.0033	699.5	45.0	710.8	19.7	621.0	115.3
4-8	167.49	95.94	0.57	0.953	0.081	0.1140	0.0033	0.0603	0.0036	676.1	43.3	696.0	19.1	563.0	143.5
4-9	120.99	69.95	0.58	0.988	0.106	0.1077	0.0029	0.0659	0.0059	689.9	53.7	659.2	16.7	757.7	172.2
5-1	136.58	54.50	0.40	0.990	0.092	0.1111	0.0033	0.0642	0.0042	693.8	46.9	679.3	19.0	691.6	147.1
5-2	136.29	60.99	0.45	0.941	0.093	0.1062	0.0033	0.0642	0.0051	667.5	48.2	650.8	19.2	672.1	169.0
5-3	142.67	68.17	0.48	0.937	0.097	0.1107	0.0033	0.0614	0.0052	664.5	52.1	676.9	19.4	549.7	210.7
5-5	211.38	137.82	0.65	1.096	0.100	0.1144	0.0032	0.0696	0.0049	746.6	47.9	698.3	18.6	858.6	145.8
5-6	124.45	61.95	0.50	1.182	0.105	0.1125	0.0041	0.0768	0.0057	797.1	43.1	687.2	23.8	1101.1	133.8
5-7	152.64	74.22	0.49	0.914	0.089	0.1087	0.0031	0.0611	0.0046	653.9	48.3	665.4	18.2	562.8	180.4
5-8	152.60	65.07	0.43	0.978	0.092	0.1112	0.0032	0.0638	0.0043	687.5	47.2	679.5	18.5	677.2	148.6
5-9	154.44	98.43	0.64	0.976	0.084	0.1112	0.0030	0.0638	0.0038	687.6	44.0	679.8	17.5	688.4	132.1
6-1	154.34	67.79	0.44	0.980	0.098	0.1163	0.0033	0.0613	0.0045	687.5	48.2	709.1	19.0	581.0	157.9
6-2	239.45	172.49	0.72	0.954	0.079	0.1103	0.0032	0.0630	0.0032	677.2	41.9	674.2	18.6	704.1	99.5
6-4	164.75	94.32	0.57	1.045	0.090	0.1200	0.0036	0.0635	0.0035	722.6	45.2	730.5	20.8	717.5	106.8
6-7	156.33	79.15	0.51	0.927	0.080	0.1115	0.0032	0.0608	0.0037	662.8	42.0	681.2	18.5	586.5	132.5
7-1	175.96	97.44	0.55	0.930	0.083	0.1117	0.0030	0.0609	0.0039	663.5	44.0	682.3	17.5	578.6	148.0
7-5	202.70	121.43	0.60	0.937	0.080	0.1107	0.0033	0.0621	0.0036	668.1	42.3	676.6	19.0	634.3	129.4
7-7	154.47	66.26	0.43	0.941	0.101	0.1097	0.0038	0.0633	0.0059	665.7	53.5	670.6	22.2	603.9	212.7
7-8	185.10	96.12	0.52	0.916	0.086	0.1136	0.0032	0.0592	0.0042	655.4	45.5	693.7	18.6	504.6	165.7
8-4	253.87	170.76	0.67	0.975	0.078	0.1129	0.0032	0.0635	0.0033	688.6	40.9	689.6	18.7	687.5	117.6
8-7	155.47	82.20	0.53	0.939	0.077	0.1085	0.0031	0.0645	0.0031	669.6	40.9	664.0	17.8	729.2	99.0
9-1	125.25	70.38	0.56	0.916	0.082	0.1116	0.0036	0.0606	0.0041	656.1	43.4	681.6	20.9	610.7	128.4
9-4	152.30	68.22	0.45	0.998	0.085	0.1193	0.0033	0.0615	0.0033	699.4	43.8	726.6	19.1	647.8	111.8
9-5	166.92	74.72	0.45	0.947	0.087	0.1162	0.0033	0.0600	0.0043	672.2	44.9	708.5	18.8	543.4	149.5
10-1	158.18	79.02	0.50	0.901	0.077	0.1071	0.0032	0.0619	0.0035	649.0	40.8	655.5	18.7	630.8	121.2
10-2	175.52	86.21	0.49	0.981	0.073	0.1135	0.0034	0.0637	0.0030	692.4	37.2	693.0	19.6	705.8	96.5
10-4	174.57	80.30	0.46	0.992	0.081	0.1158	0.0032	0.0629	0.0030	696.8	40.2	706.1	18.7	678.1	99.7
10-6	134.16	66.29	0.49	1.035	0.105	0.1094	0.0032	0.0695	0.0053	714.5	51.6	669.0	18.7	844.8	158.8
10-7	104.33	41.17	0.39	0.973	0.100	0.1118	0.0035	0.0639	0.0051	683.2	51.5	683.1	20.5	658.7	173.2
10-9	106.03	45.48	0.43	0.963	0.089	0.1165	0.0037	0.0607	0.0040	680.0	46.8	710.1	21.1	563.9	163.4
11-5	168.11	81.34	0.48	0.869	0.081	0.1076	0.0028	0.0588	0.0037	630.6	43.9	658.6	16.2	505.0	143.9

Table 3: LA-ICP-MS single zircon Lu–Hf isotopic data of sample OS-69 from the Sukari granite intrusion.

Grain	t (Ma)	$^{176}\text{Yb}/^{177}\text{Hf}$	2σ	$^{176}\text{Lu}/^{177}\text{Hf}$	2σ	$^{176}\text{Hf}/^{177}\text{Hf}$	2σ	Hf(i)	ϵHf_t	2σ	T _{DM}	T _{DM} ^c
1-1	678	0.142163	0.002208	0.003376	0.000021	0.282795	0.000052	0.282850	16.2	1.85	608	574
1-2	673	0.130838	0.001042	0.004088	0.000016	0.282770	0.000052	0.282826	15.0	1.84	658	650
1-3	688	0.137388	0.001344	0.003233	0.000015	0.282719	0.000051	0.282774	13.6	1.82	720	741
1-5	682	0.086527	0.000908	0.002153	0.000005	0.282710	0.000051	0.282766	13.8	1.81	711	729
1-6	672	0.092513	0.000525	0.002165	0.000015	0.282652	0.000051	0.282757	13.4	1.82	723	749
1-7	682	0.174552	0.000264	0.004154	0.000029	0.282797	0.000051	0.282852	15.9	1.82	619	593
1-8	696	0.134912	0.000778	0.003365	0.000013	0.282744	0.000051	0.282799	14.4	1.82	685	689
1-9	697	0.112880	0.000661	0.003494	0.000010	0.282738	0.000051	0.282793	14.1	1.82	696	706
1-10	679	0.100613	0.002087	0.002468	0.000030	0.282739	0.000051	0.282794	14.6	1.82	676	675
2-1	669	0.203450	0.004120	0.004607	0.000097	0.282945	0.000051	0.282800	13.9	1.82	709	723
2-2	676	0.138000	0.004208	0.003588	0.000070	0.282861	0.000051	0.282816	14.9	1.81	664	658
2-3	672	0.149132	0.003335	0.003704	0.000051	0.282869	0.000052	0.282724	11.6	1.82	806	867
2-4	664	0.145822	0.002865	0.003523	0.000051	0.282818	0.000054	0.282773	13.4	1.92	727	751
2-5	667	0.073193	0.000872	0.001801	0.000008	0.282705	0.000051	0.282760	13.7	1.81	712	732
2-7	718	0.110830	0.000623	0.002729	0.000020	0.282804	0.000051	0.282759	13.3	1.82	732	761
2-9	680	0.137345	0.004460	0.003624	0.000060	0.282933	0.000054	0.282788	13.9	1.92	707	722
2-10	659	0.103987	0.000440	0.002596	0.000025	0.282644	0.000051	0.282799	14.7	1.82	671	668
3-1	690	0.093169	0.001102	0.002193	0.000008	0.282668	0.000051	0.282752	13.3	1.82	731	761
3-2	669	0.154864	0.007585	0.003314	0.000129	0.282911	0.000051	0.282766	13.3	1.82	733	762
3-4	678	0.099983	0.000609	0.002459	0.000005	0.282839	0.000051	0.282794	14.6	1.82	675	675
3-5	672	0.123862	0.001906	0.003599	0.000013	0.282810	0.000051	0.282785	13.8	1.81	711	727
3-7	697	0.137054	0.000726	0.003352	0.000013	0.282761	0.000051	0.282816	15.0	1.82	659	651
3-8	690	0.100065	0.003955	0.002502	0.000082	0.282737	0.000051	0.282792	14.5	1.82	679	680
4-1	651	0.134682	0.000916	0.003145	0.000009	0.282820	0.000051	0.282775	13.6	1.82	717	737
4-2	711	0.099777	0.001015	0.002390	0.000008	0.282733	0.000051	0.282787	14.4	1.81	684	687
4-3	697	0.073496	0.000835	0.002088	0.000011	0.282761	0.000051	0.282782	14.3	1.81	687	692
4-4	679	0.137360	0.001617	0.003001	0.000004	0.282637	0.000051	0.282692	10.7	1.82	838	920
4-5	677	0.124562	0.000786	0.002869	0.000007	0.282780	0.000051	0.282835	15.9	1.82	623	595
4-7	711	0.139307	0.001357	0.003656	0.000002	0.282856	0.000051	0.282711	11.1	1.82	825	896
4-8	696	0.174602	0.005929	0.004800	0.000144	0.282613	0.000052	0.282768	12.6	1.83	763	800
4-9	659	0.115898	0.002321	0.002984	0.000040	0.282751	0.000052	0.282806	14.8	1.85	668	663
5-1	679	0.121532	0.000721	0.002797	0.000004	0.282837	0.000051	0.282791	14.4	1.82	686	691
5-2	651	0.178538	0.008569	0.004009	0.000112	0.282824	0.000051	0.282778	13.4	1.82	730	755
5-3	677	0.149628	0.008414	0.003225	0.000132	0.282869	0.000051	0.282723	11.8	1.82	797	856
5-5	698	0.095509	0.000319	0.002366	0.000010	0.282734	0.000051	0.282758	13.4	1.82	726	753
5-6	687	0.115038	0.001359	0.002814	0.000012	0.282832	0.000051	0.282786	14.2	1.82	693	702
5-7	665	0.144675	0.001113	0.003460	0.000023	0.282825	0.000051	0.282779	13.6	1.82	718	738
5-8	679	0.111496	0.000404	0.002721	0.000015	0.282782	0.000051	0.282754	13.1	1.82	740	773
5-9	680	0.118685	0.001201	0.002887	0.000006	0.282728	0.000051	0.282783	14.0	1.82	700	713
6-1	709	0.113279	0.001688	0.003153	0.000009	0.282759	0.000051	0.282814	15.0	1.82	659	651
6-2	674	0.183749	0.001711	0.004603	0.000081	0.282826	0.000051	0.282788	13.4	1.82	727	749
6-4	731	0.232084	0.001003	0.006386	0.000118	0.282929	0.000051	0.282783	12.5	1.82	775	811
6-7	681	0.136423	0.002001	0.004261	0.000029	0.282810	0.000052	0.282756	12.5	1.83	769	811
7-1	682	0.093788	0.000288	0.002354	0.000009	0.282731	0.000051	0.282764	13.6	1.82	717	738
7-5	677	0.127373	0.001836	0.003762	0.000020	0.282799	0.000052	0.282753	12.6	1.83	763	803
7-7	671	0.172805	0.004275	0.003804	0.000039	0.283002	0.000052	0.282756	12.7	1.83	760	800
7-8	694	0.091937	0.001286	0.002553	0.000009	0.282724	0.000051	0.282778	14.0	1.81	701	714
8-4	690	0.144280	0.004281	0.003766	0.000066	0.282903	0.000051	0.282757	12.7	1.82	757	795
8-7	664	0.149458	0.003740	0.003704	0.000055	0.282868	0.000051	0.282722	11.5	1.81	809	872
9-1	682	0.122508	0.001311	0.002855	0.000045	0.282779	0.000052	0.282783	14.1	1.83	699	710
9-4	727	0.130050	0.001126	0.003206	0.000010	0.282891	0.000051	0.282764	13.2	1.82	734	763
9-5	708	0.145892	0.001272	0.003775	0.000025	0.282891	0.000051	0.282785	13.7	1.81	715	734
10-1	655	0.071617	0.000688	0.001746	0.000007	0.282732	0.000051	0.282786	14.6	1.82	674	673
10-2	693	0.116402	0.000712	0.002786	0.000011	0.282856	0.000051	0.282761	13.3	1.82	730	758
10-4	706	0.101570	0.001480	0.002381	0.000023	0.282806	0.000051	0.282786	14.4	1.82	686	690
10-6	669	0.121096	0.004461	0.002811	0.000060	0.282804	0.000051	0.282786	14.2	1.82	694	703
10-7	683	0.069003	0.001251	0.001725	0.000018	0.282698	0.000051	0.282752	13.5	1.82	722	748
10-9	710	0.081767	0.000883	0.002447	0.000013	0.282736	0.000051	0.282789	14.5	1.81	682	685
11-5	659	0.168172	0.006232	0.004773	0.000081	0.283041	0.000052	0.282794	13.6	1.84	721	740

5.4. Zircon trace elements

Trace elements of zircons from sample OS-69 are presented in (Table 4). There are significant variations in some elements including Hf (7132–9754 ppm), Zr (466254–549605 ppm), Ta (1.26–4.99 ppm), Y (2159–49944 ppm), Nb (5.6–26.5 ppm), Ti (1.7–1959 ppm), U (97–314 ppm), Th (36–202 ppm) and total REE (1308–29640 ppm). The Zr/Hf ratios in the studied zircons vary between 51 and 69 (average = 59.4), which are higher than chondritic values (~35–40, [77]) but are similar to zircons from felsic igneous rocks [78–80]. Chondrite-normalized REE patterns of the analysed zircons are presented in (Figure. 9a). The zircons show positive Ce- and negative Eu-anomalies ranging from 0.93 to 81.23 (average = 24.43) and 0.16 to 0.36 (average = 0.22), respectively. The $(La/Yb)_N$ ratios are lower than 0.23 in all grains indicating HREE enrichment relative to LREE. The +ve Ce anomalies characterize magmatic zircons [81–84]. Compared to chondritic abundance, few zircon grains (no. 1-1, 1-3, 4-9, 5-5, 5-7, 9-5, (Table 4 and Figure. 9a) display overabundance of LREEs $\{(La)_N=314 - 2407\}$ that exceed the normal range of igneous zircons [82], nearly flat REE patterns, and absence of Ce positive anomalies (Figure. 9a). These criteria may reflect hydrothermal origin of these zircon grains [85]. Except for the above-mentioned zircon grains, the Ce contents in the remaining grains are relatively high as represented by their Ce-positive anomalies. This may indicate an oxidized magma with abundant tetravalent Ce. The negative Eu-anomalies in the different analysed zircons (Figure. 9a) characterize highly fractionated granite as in the whole rock REE patterns [84]. The negative Eu anomalies in all grains imply the role of feldspar fractionation during zircon crystallization [81, 86–89]. The MREEs in the analysed zircons are slightly enriched whereas the HREEs and Y have typical range of 10^3 and 10^4 chondrite [71, 82, 90]. The Y concentrations in the Sukari zircons (2159–49944 ppm) are similar to those in zircons from other granitoids (71, 82, 90–93).

In the last three decades, Ti-in-zircon thermometry has been applied to zircons [78, 90, 92, 94–102]. Based on experimental work [103–105], Ti in the crystal lattice of zircon depends on the activity of TiO_2 (a_{TiO_2}) and temperature. The calculated crystallization temperatures of zircons from the Sukari granite are shown in (Table 4). This thermometer depends on titania activity (a_{TiO_2}) and silica activity (a_{SiO_2}), which depend on rutile and quartz saturation, respectively. Quartz occurs in the analysed sample, and therefore, a_{SiO_2} is considered to equal 1.0 [106–107]. The Ti-in-zircon thermometer is best applied in systems containing pure TiO_2 phase, such as rutile and/or ilmenite [108–109]. Ilmenite is common in the studied sample OS-69 of the Sukari granite from which zircon was separated, and it contains high percentage of TiO_2 (0.15 wt%). Thus, a value for a_{TiO_2} equal 0.9 is recommended [106] during the crystallization of zircon from the Sukari granite.

Five grains (4-2, 5-8, 5-9, 6-4, 8-4, Table 4) yielded high temperatures (1780 – 972°C), which may be attributed to their unusual anomalous Ti content. Such high Ti contents are not workable for primary igneous zircon and could be altered zircon or zircon hosting Ti-rich inclusions (e.g. rutile). Accordingly, these points are ignored when calculating the average temperature. The remaining points show zircon

crystallization temperatures in the range of 606 – 819°C (average = 702°C). (Figure. 9b) show the Hf contents in the studied zircon plotted against the crystallization temperatures where a gradual decrease in temperatures with increasing Hf is shown. This could be attributed to zircon/melt Hf/Zr fractionation during magmatic evolution (Figure. 9b). Except the 5 grains that yield extremely high temperatures, all grains lie within the range of unaltered magmatic zircon (Figure. 9b).

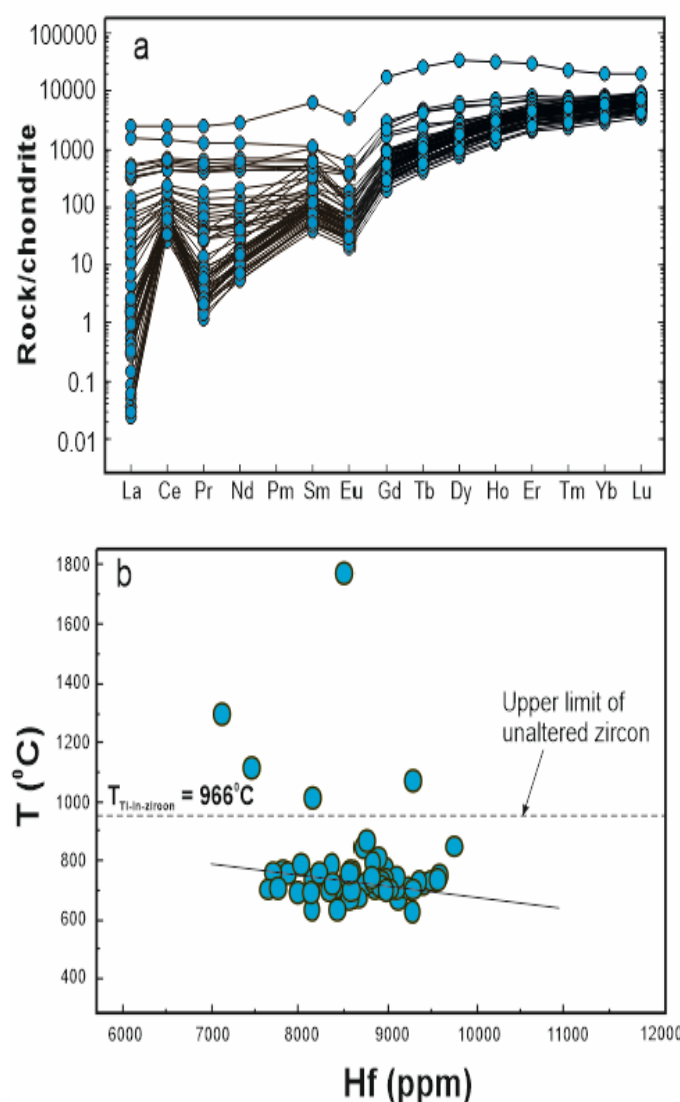


Figure 9. (a) Chondrite-normalized REE patterns for zircons of sample OS-69 from the Sukari granite (normalization values are from [59]), (b) Plot of the calculated crystallization temperatures of the studied zircon grains against their Hf contents. The boundary value of maximum Ti abundance in unaltered igneous zircon is after [82].

Table 4: Trace elements (ppm) for zircon grains of sample no. OS-69 from the Sukari granite intrusion.

Grain	La	Ce	Pr	Nd	Sm	Eu	Gd	Tb	Dy	Ho	Er	Tm	Yb	Lu	Hf	Ta	Ti	Y	Zr	Nb	Th	U	Li	Si	Sc	T°C
1-1	127.04	423.81	61.85	327.49	102.29	8.64	205.24	53.49	561.40	196.54	821.98	146.65	1128.98	203.26	8829	1.67	5.19	5846	545104	8.61	84.10	172.78	4.70	158483	420.30	694
1-2	0.34	49.21	0.34	5.27	11.21	1.98	83.38	30.02	362.51	134.49	586.26	108.77	852.50	153.68	9007	3.88	4.28	4058	549605	15.95	72.00	195.13	5.08	157700	421.50	678
1-3	570.56	1553.81	234.73	1302.53	996.29	201.37	3646.59	1009.23	8777.47	1866.98	4911.48	573.71	3484.16	511.11	8979	2.39	9.23	49944	543459	9.36	174.17	181.94	5.65	160551	426.47	747
1-5	0.07	33.39	0.96	17.89	67.65	20.22	380.84	98.68	750.49	189.72	683.90	111.17	820.03	145.33	8529	2.91	5.28	5629	543878	11.84	73.54	162.26	2.93	155930	426.58	696
1-6	0.01	34.96	0.24	4.67	13.24	2.54	99.81	33.97	412.16	153.01	667.48	118.22	928.89	166.92	9171	1.77	4.41	4555	540034	7.26	55.53	138.74	6.58	159538	432.98	681
1-7	24.63	118.85	10.90	50.59	47.12	11.09	183.59	51.05	491.79	168.82	708.41	123.72	943.34	167.14	8674	3.72	4.89	4996	535795	17.85	84.31	203.60	3.51	165181	432.66	689
1-8	14.39	77.98	7.41	41.94	21.75	2.82	93.52	31.59	375.07	139.15	599.24	108.05	825.31	153.14	9396	2.75	5.39	4130	535187	10.88	60.65	157.81	5.30	160898	433.26	698
1-9	1.04	21.31	0.82	8.61	15.31	3.08	105.74	36.87	438.05	159.21	690.65	121.59	939.71	175.11	8861	1.26	4.24	4824	529389	5.64	54.88	127.40	4.01	162991	438.14	677
1-10	0.02	39.56	0.25	5.30	13.90	2.88	100.51	36.54	442.22	159.43	708.74	126.62	958.30	174.70	9108	2.71	2.77	4863	523684	12.38	64.71	162.29	3.76	160516	434.60	643
2-1	93.22	322.86	45.05	244.14	76.64	6.81	161.24	44.10	480.08	163.75	710.37	124.23	952.97	170.79	9492	2.59	6.06	4911	519163	12.00	73.32	169.32	4.50	159560	440.37	708
2-2	7.40	74.79	5.13	33.77	33.71	4.88	160.68	54.46	603.21	210.86	932.04	164.08	1267.93	230.14	8727	3.75	17.48	6503	523700	20.59	157.25	269.25	2.98	166844	442.42	812
2-3	3.15	65.90	2.48	27.21	81.02	21.67	536.09	180.99	1608.90	412.54	1379.59	204.43	1394.32	233.96	8739	3.97	5.19	12599	519172	18.34	187.55	269.18	3.49	157259	432.64	694
2-4	0.01	44.78	0.22	5.21	16.25	3.08	116.69	42.28	529.59	187.46	830.61	147.04	1124.61	198.19	9231	2.02	4.71	5739	508747	9.34	70.72	161.72	9.34	157754	428.28	686
2-5	0.46	38.91	0.41	4.75	9.98	1.83	70.34	25.21	314.87	117.71	525.36	93.37	729.50	130.41	8664	3.38	3.12	3544	515216	14.66	81.56	173.44	3.54	163655	433.72	652
2-7	27.38	119.09	13.02	71.30	25.83	3.12	79.13	25.66	299.32	110.91	493.25	87.79	675.80	121.13	9278	3.55	1.69	3329	513860	13.58	77.72	183.93	4.99	165261	427.80	606
2-9	0.37	36.42	0.55	6.98	16.49	2.97	107.12	37.80	466.15	171.59	773.28	134.46	1036.11	180.98	8158	2.12	1.85	5195	514510	9.92	74.74	167.82	5.65	141787	437.84	613
2-10	0.01	30.89	0.24	4.49	11.79	2.23	83.89	30.19	370.51	137.15	628.16	111.15	889.61	157.80	9358	2.25	5.70	4158	512923	10.53	57.43	149.16	4.04	158417	429.66	703
3-1	0.38	18.63	0.32	3.91	9.69	1.72	62.94	22.82	288.73	107.51	496.38	87.41	703.43	125.73	9094	1.76	4.29	3261	506737	6.61	46.61	111.15	3.24	160360	421.91	678
3-2	17.63	85.67	8.60	52.87	23.46	3.12	101.85	33.91	392.64	142.78	648.74	112.62	889.55	152.02	9594	2.38	7.00	4327	508423	10.14	61.33	146.37	4.61	156275	421.19	721
3-4	0.19	47.48	0.29	5.43	15.22	2.74	101.60	34.97	440.02	161.19	738.06	132.01	1025.60	175.61	9100	3.17	6.69	4950	511493	13.85	71.51	181.64	6.15	164483	430.36	717
3-5	0.10	42.06	0.31	5.77	14.72	2.99	102.35	36.68	444.40	165.42	740.50	130.57	1046.32	180.70	8893	3.70	12.75	5029	499119	18.89	104.49	210.23	3.42	156847	416.63	779
3-7	12.19	65.52	6.18	35.14	14.93	1.83	56.23	18.97	233.50	91.39	430.00	77.80	652.62	115.40	9754	2.95	18.71	2764	498503	12.49	36.11	112.67	2.52	154517	412.54	819
3-8	0.48	15.53	0.23	2.64	6.03	1.15	40.37	14.69	182.47	71.05	326.32	59.35	496.84	90.49	8985	1.64	6.29	2159	502112	5.99	37.34	96.88	2.71	156780	419.37	711
4-1	0.24	31.01	0.25	5.11	13.44	2.06	87.20	31.45	381.74	145.15	635.51	113.87	890.62	157.15	9564	1.77	6.51	4361	495156	7.64	63.41	144.26	5.43	148648	415.86	714
4-2	0.61	25.81	0.57	7.92	18.46	4.16	104.91	36.24	395.29	140.08	606.66	103.08	831.49	147.67	8563	2.58	1958.60	4238	497661	19.56	69.11	146.34	2.47	166250	428.36	1780
4-3	0.07	38.83	0.21	5.22	13.21	2.46	90.31	31.75	385.13	143.88	636.97	114.18	914.84	162.57	8566	2.75	2.80	4405	497220	11.39	68.62	165.17	3.41	157674	416.99	644
4-4	0.01	36.13	0.20	6.06	16.52	2.90	106.63	39.20	451.21	169.21	736.89	130.12	1036.66	183.28	8848	1.93	5.60	5077	493771	7.79	67.01	154.75	6.64	156403	410.78	701
4-5	0.40	39.14	0.54	9.41	20.09	3.36	136.02	48.78	578.77	217.16	935.54	162.37	1267.01	223.83	8933	1.96	5.44	6414	498630	9.93	90.63	194.86	6.09	151644	409.44	699
4-7	7.91	64.39	4.11	24.15	14.45	2.20	73.80	26.80	313.81	121.94	535.65	94.67	780.91	141.10	9024	3.60	4.41	3610	497206	14.14	62.44	170.14	2.59	158873	406.63	681
4-8	8.10	56.12	3.71	22.95	18.60	4.03	101.54	34.97	382.41	141.85	615.04	110.58	877.45	158.83	8823	3.16	11.74	4312	484691	13.51	101.40	183.53	4.52	158847	409.66	770
4-9	80.07	261.80	37.60	158.00	34.98	624.99	170.80	1320.48	347.60	1172.77	185.74	1367.41	225.15	8763	2.69	21.78	10472	490894	14.13	97.99	174.26	4.04	152872	411.56	836	
5-1	0.14	33.58	0.21	3.59	7.88	1.56	57.16	21.33	266.99	105.17	447.32	81.50	668.96	121.59	9294	3.21	4.36	3106	490541	12.31	55.66	144.58	3.92	151116	409.76	680
5-2	0.32	35.41	0.57	11.80	33.15	8.23	193.80	63.39	611.04	195.88	738.95	125.22	966.02	168.88	8948	2.17	4.76	5840	489205	9.59	63.16	146.51	5.38	149024	405.96	687
5-3	0.08	26.95	0.40	7.18	15.52	2.95	107.84	40.37	476.48	177.88	757.12	137.70	1070.27	195.11	8414	1.62	3.92	5417	487744	7.06	67.24	147.34	6.91	150190	404.86	671
5-5	371.78	916.95	117.46	580.99	168.40	20.04	338.54	84.44	761.85	227.95	847.22	144.33	1103.46	195.90	7828	3.72	8.74	6971	490068	18.22	159.11	244.09	3.26	157999	418.15	742
5-6	0.36	25.02	0.46	7.53	15.58	2.85	98.66	34.53	421.50	157.25	661.08	118.98	934.76	167.51	8382	1.98	10.05	4732	493532	11.17	69.09	144.70	4.29	153344	406.65	755
5-7	74.52	270.89	38.22	205.42	64.86	6.75	158.16	45.88	508.01	178.30	752.73	134.63	1069.67	195.74	8580	2.28	4.12	5381	494492	9.31	74.39	159.74	4.77	151438	415.20	675
5-8	8.16	108.99	3.73	20.44	14.24	2.65	82.24	29.79	382.94	136.41	582.70	104.47	809.70	145.18	8165	3.66	63.33	4193	494402	15.47	71.79	175.64	3.21	161698	410.95	972
5-9	3.50	62.72	3.55	46.60	99.59	21.37	452.32	155.27	1395.36	342.44	1150.02	174.42	1222.70	205.82	7132	4.20	296.88	10766	486673	22.55	153.79					

6. Discussion

6.1. Post-magmatic alteration

The Sukari granite is a gold-mineralized pluton, which was intruded into an island arc metavolcano-sedimentary succession and ophiolitic melange assemblage. The mineralization occurs mainly as a grid of quartz veins surrounded by intensely altered wall rock along NE-SW shear zones containing sulphidized, silicified, and sericitized rocks [32, 36]. Sericite from the altered rocks yields $^{40}\text{Ar}/^{39}\text{Ar}$ age of $\sim 625 \pm 3$ Ma, which has been attributed to the onset of major sinistral transpression in the region [32]. In many places, the Sukari granite itself is widely affected by hydrothermal alteration where sericite and calcite are major alteration mineral (Figure. 2e). However, careful selection of fresh samples in the present study, as indicated by the small values of loss on ignition (LOI=1.90–3.50 wt%, Table 1) reflects the low to negligible degrees of hydrothermal alteration. In addition, the absence of wide variations in the mobile LILEs Rb (10-69 ppm, average=34 ppm), Sr (17-72 ppm, average=33 ppm), and Ba (53-365 ppm, average=240 ppm) indicate a weak influence of chemical alteration. Moreover, the trace elements of zircons from the Sukari granite demonstrate that they have Th/U (0.32-0.96), Zr/Hf (51-69), positive Ce and negative- Eu-anomalies like those reported for zircons from highly evolved igneous rocks [78-84]. The evaluation of the mobility of elements during hydrothermal alteration can be assessed by Zr as it is broadly considered as immobile element [110]. Zr shows good correlations against mobile elements such as K, Sr, Rb, and Ba (Figure. 10), which may suggest that hydrothermal alteration is insignificant and thus the collected samples are suitable for age dating and geochemical analyses.

6.2. Evolutionary mechanism of the Sukari granite

Petrographic variations within the Sukari trondhjemite-granodiorite-granite suite indicate that it had evolved mainly by fractional crystallization. The observed euhedral plagioclase phenocrysts in the Sukari granites suggest that fractionation was a significant process during the evolution of the pluton. Most samples show negative correlation between CaO, MgO, Al_2O_3 , Fe_2O_3 , Sr contents and SiO_2 (Figure. 4) that can be described by the removal of plagioclase and ferromagnesian minerals from the melt. The negative Eu, Ba and Sr anomalies (Figure. 5) could be also suggestive of the removal of feldspars from the magma. However, the increasing of K₂O, Rb, Ba and decreasing of Sr with increasing the strongly incompatible element Zr (Figure. 10) suggests the major role of plagioclase fractionation. Moreover, The Nb, Ta and Ti anomalies (Figure. 5a) could be attributed to fractionation of Nb-bearing minerals such as amphibole. (Figures. 11a and b) are binary plots of Sr vs. Ba and SiO_2 vs. Eu/Eu* where elemental variations on these diagrams define linear trends indicating that the Sukari granite has mainly evolved by fractional crystallization. Also, the robust Zr/Ti fractionation index covaries very strongly with high field strength elements (HFSEs) like U (Figure. 11c). Such geochemical variation between Zr/Ti and U indicates that all samples are co-genetic, and their evolution is mainly controlled by fractional crystallization of feldspars and ferromagnesian minerals from the one parent magma.

The linear correlation shown by most samples of the Sukari granite can also be regarded as due to variable degrees of partial melting. The strongly compatible and incompatible elements and their ratios are generally used to evaluate the evolution processes of felsic igneous rocks [111-114].

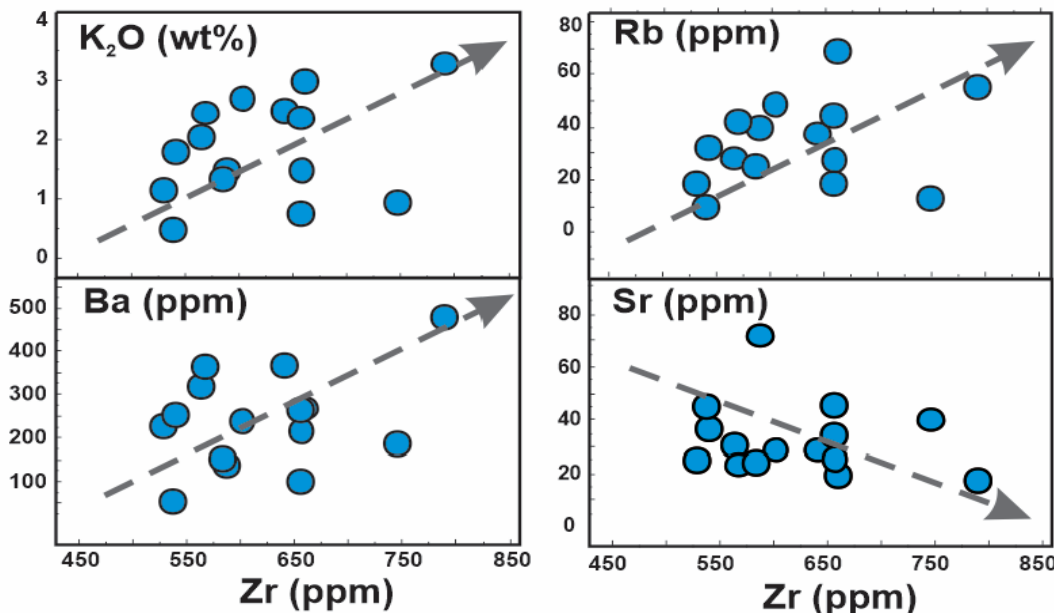


Figure 10. Variation of Zr vs. K₂O, Rb, Ba, and Sr for the Sukari granites. Arrows are visual estimate of the evolutionary trends.

The data of the Sukari granite are plotted on Zr vs. Zr/Nb diagram and Th vs. Th/Ta (**Figures. 11d and e**) where the trends are more consistent with fractional crystallization processes and opposed to variable degrees of partial melting. The involvement of a crustal source did not play a significant role in the evolution of the Sukari granite.

The absence of inherited zircons together with the linear trends in the diagrams of SiO_2 vs. some elements (**Figure. 4**) suggests that crustal contribution was not a major mechanism in the evolution of the Sukari granite. Also, the positive and limited variation in $\epsilon\text{Hf}_{\text{T}}$ (+10.7 to +16.2, **Figure. 8**) is similar to rocks expected to be generated from depleted source without significant crustal contamination from old continental crust.

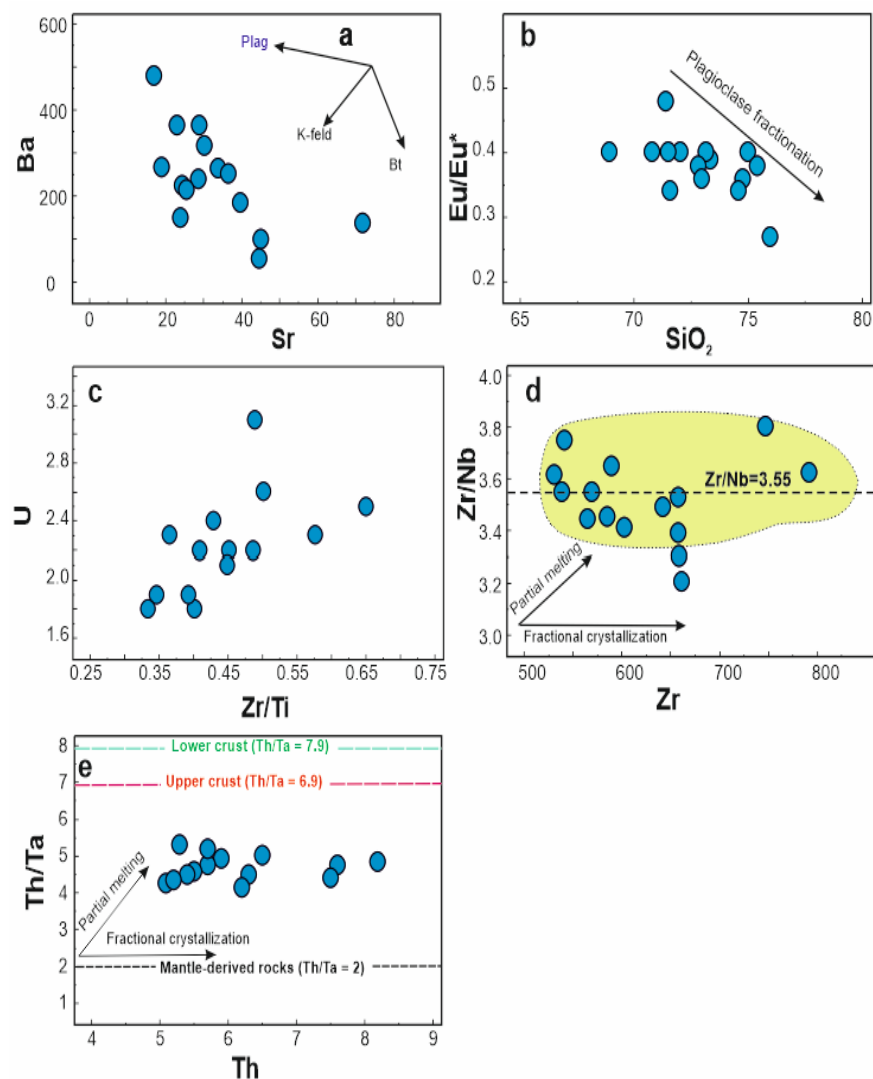


Figure 11. Plots of: (a) Sr vs. Ba, (b) SiO_2 vs. Eu/Eu^* , (c) Zr/Ti vs. U, (d) Zr vs. Zr/Nb , and (e) Th vs. Th/Ta for the Sukari granite. Arrows in figure a indicate the trends of fractionation of plagioclase feldspar (plag), K-feldspar (K-feld) and biotite (Bt). The trends of partial melting and fractional crystallization are according to [113].

6.3. Source of the Sukari granite magma

The origin of subduction-related calc-alkaline trondhjemite-granodiorite-granite suites all over the world was explained by extensive fractionation of mantle- or mafic lower crust-derived partial melts [115-122]. The Sukari granites show chemical composition of low K_2O (average = 1.84 wt%) and Rb (average = 34 ppm) consistent with their origin by partial melting of a depleted source [123]. Since the lower and upper continental crust have Th/Ta ratios of 7.9 and 6.9, respectively, while the mantle-derived rocks have ratios close to 2 [124], the Th/Ta ratios are considered as crucial indicators of the contribution of mantle and crust sources. The Th/Ta ratios in the studied granite vary between 4.13 to 5.0 (average = 4.67) and are in between those of the crust and mantle values indicating mantle source with crustal contribution. Similarly, the Sukari granite has Ba/Rb ratios between 3.46 and 14.38 (average 7.71), which are fairly similar to mantle estimate ($Ba/Rb = 11$) [125] and higher than crustal estimate ($Ba/Rb = 6.7$) [126]. This is again implying the contribution of mantle-derived melt in the genesis of the Sukari granite. Moreover, in the Sr/Y - Y and La/Yb - Yb diagrams (**Figures. 12a and b**), the Sukari granite is mostly plotted in the field of volcanic arc rocks as it possesses low Sr/Y and La/Yb values [127-128]. This suggests that the mafic lower crust alone was not the likely source of the Sukari granite [129] but as in all arc rock, it was formed by partial melting of a mantle source with the involvement of lower crust materials through metasomatic processes.

The subduction-related 676.5 Ma age Sukari granite have zircons with $\epsilon Hf(T)$ between +10.7 to +16.2 (**Table 3**). Such values are consistent with previous zircon Lu-Hf isotope studies of granites in the Eastern Desert and Sinai ($\epsilon Hf(T) = +5.5$ to +113.9) [75-76, 130-131] and validates the hypothesis that the original source of the Sukari granite magma was depleted. The single-stage Hf model ages (HfT_{DM}) offer the lowest estimates for the formation of crust [132]. The HfT_{DM} values calculated for the 676.5 Ma Sukari granite are between 0.61 - 0.84 Ga (average 0.71 Ga) whereas the two-stage Hf model age (T_{DM}^c) are between 0.57 – 0.92 Ga (average 0.73 Ga). The HfT_{DM} and HfT_{DM}^c ages agree with the accepted age of formation of the ANS [1, 131], which indicates a negligible contribution from a pre- Pan-African crust and the derivation of the Sukari granite by partial melting of a juvenile source. According to [76, 133], Lu-Hf isotopic compositions of rocks from the ANS that yield $Hf-T_{DMc} = t$ (t is the U-Pb zircon age) or $Hf-T_{DMc} < t + 300$ reflect a juvenile source. On the other hand, rocks with $t + 300 < Hf-T_{DMc} < t + 900$ reflect juvenile source with crustal contamination by pre-Pan-African crust, and those with $Hf-T_{DMc} > t + 900$ are derived from evolved pre-Pan-African crust. The Sukari granite yielded $Hf-T_{DMc} = t$ (**Figure. 13**), which suggest that its magma was derived from a juvenile source. This source could be interpreted as a mixture between depleted mantle and juvenile crust.

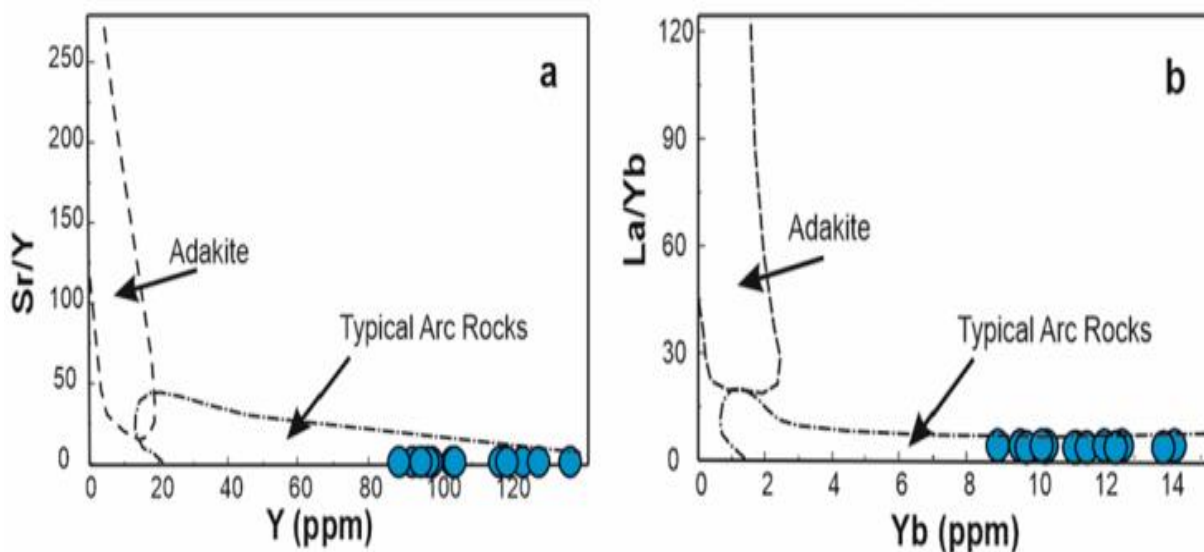


Figure 12. Plots of (a) Sr/Y versus Y and (b) La/Yb versus Yb for the Sukari granite pluton with the fields for adakite and island arc rocks from [127].

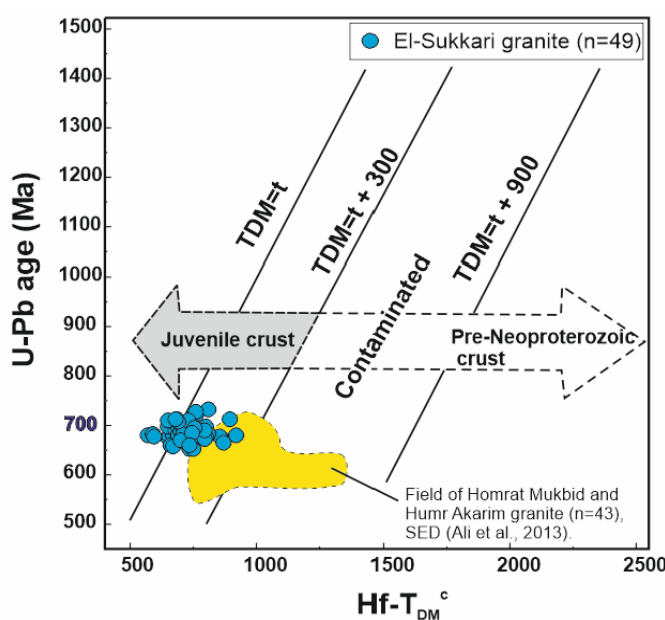


Figure 13. U-Pb zircon ages versus Hf model ages (Hf-T_{DMc}), modified after [76, 133], for single zircons from the Sukari granite intrusion in the South Eastern Desert of Egypt. Model ages were calculated assuming a mean $^{176}\text{Lu}/^{177}\text{Hf}$ value of 0.015 for average continental crust [55]. Data yielding $\text{Hf-T}_{\text{DMc}} = t$ (U-Pb zircon age) or $\text{Hf-T}_{\text{DMc}} < t + 300$ are considered to come from juvenile oceanic crust, whereas those with $t + 300 < \text{Hf-T}_{\text{DMc}} < t + 900$ are considered from juvenile crust contaminated by pre-Neoproterozoic crust, and those with $\text{Hf-T}_{\text{DMc}} > t + 900$ are from evolved (continental) pre-Neoproterozoic crust.

7. Conclusions

In this work, we performed a whole rock geochemical study coupled with zircon U-Pb-Hf isotopes and trace elements analyses for the Sukari granite intrusion in the CED of Egypt. The following conclusions can be presented:

- The Sukari granites represent a trondhjemite-granodiorite-granite suite and is characterized by the occurrence of porphyritic, granophytic and equigranular textural varieties. They are metaluminous to peraluminous (A/CNK molar ratios = 0.91–1.84) with calc-alkaline affinity. The geochemical characteristics of the Sukari granites are most likely similar to I-type, subduction-related magmatism.
- Zircons from the Sukari granite have Th/U ratios of 0.32–0.96, Zr/Hf ratios of 51–69, positive Ce and negative Eu anomalies, HREE enrichment relative to LREE, and zircon crystallization temperatures of 606 – 819°C (average = 702°C), which are similar to those reported for zircons from highly evolved igneous rocks.

3- Zircon U-Pb isotopic dating of the Sukari granite reveals an emplacement age of 676.5 ± 1.3 Ma, reflecting its late Cryogenian age and thus it belongs to the Egyptian syntectonic older granite group. Zircon Lu-Hf isotopic composition show $\epsilon\text{Hf}(t)$ of +10.7 to +16.2, T_{DM} and T_{DMC} ages of 608–838 Ma and 574 – 920 Ma, respectively. The T_{DMC} ages are similar to the zircon U-Pb crystallization ages, which suggest a juvenile source for the Sukari granite and preclude contribution from pre-Neoproterozoic crust.

- The Lu-Hf isotopic composition and the geochemical characteristics of low K_2O (average = 1.84 wt%) and Rb (average = 34 ppm) suggest the derivation of the Sukari granite by partial melting of a depleted mantle. However, the Th/Ta and Ba/Rb ratios in the Sukari granite, which are important indication of mantle and crust contribution, show values between those of the crust and mantle indicating mantle source with crustal contribution. This suggests that the Sukari granite magma was derived mainly by partial melting of a metasomatized depleted mantle.
- Variations of SiO_2 vs. Eu/Eu^* and Sr vs. Ba define linear trends indicating that magma of the Sukari granite had evolved by fractional crystallization. Also, the Zr vs. Zr/Nb and Th vs. Th/Ta diagrams show trends more consistent with fractional crystallization. The increasing of K_2O , Rb, Ba and decreasing of Sr with increasing strongly incompatible elements such as Zr suggests the major role of plagioclase fractionation. Fractionation of amphibole and mica, which are Nb-Fe-Ti-bearing minerals, is linked to the negative anomalies in Nb, Ta, and Ti on the multi-element spiderdiagram.

Acknowledgments: This work was financially supported through a scholarship to Aya F. Harhash from Centamin Company and Michael Krewoldt Scholarship program at the Geology Department, Alexandria University. The authors would like to acknowledge the Centamin PLC for their support and for permitting and stimulating field work and sample collection. The authors are also grateful to the scholarship advisor, Prof. Hanafy Holail, for his continuous support. Thanks are due to the research team at the Sukari gold mine for the valuable advice during field work.

References

- Stern, R.J. Arc Assembly and Continental Collision in the Neoproterozoic East African Orogen: Implications for the Consolidation of Gondwanaland. *Ann. Rev. Earth Planet. Sci.* 1994, 22, 319–351.
- Kröner, A.; Muhongo, S.; Hegner, E.; Wingate, M.T.D. Single zircon geochronology and Nd isotopic systematics of Proterozoic high-grade rocks from the Mozambique belt of southern Tanzania (Masasi area): implications for Gondwana assembly. *J. Geol. Soc. London* 2003, 160, 745–757.
- Meert, J.G.; Torsvik, T.H. The making and unmaking of a supercontinent: Rodinia revisited. *Tectonophysics* 2003, 375, 261–288.
- Kröner, A.; Stern, R.J. Pan-African Orogeny. *Encyclopedia of Geology* 1, Elsevier, Amsterdam, 2004.

- [5] Gray, D.R.; Foster, D.A.; Meert, J.G.; Goscombe, B.D.; Armstrong, R.; Trouw, R.A.J.; Passchier, C.W. A Damara orogen perspective on the assembly of southwestern Gondwana. In: Pankhurst R, Trouw R, et al, eds. West Gondwana Pre-Cenozoic Correlations Across the South Atlantic Region. Geol. Soc. London, Special Publ. 2008, 294, 257–278.
- [6] Li, Z.X.; Bogdanova, S. V.; Collins, A.S.; Davidson, A.; De Waele, B.; Ernst, R.E.; Fitzsimons, I.C.W.; Fuck, R.A.; Gladkochub, D.P.; Jacobs, J.; Karlstrom, K.E.; Lu, S.; Natapov, L.M.; Pease, V.; Pisarevsky, S.A.; Thrane, K.; Vernikovsky, V. Assembly, configuration, and break-up history of Rodinia: A synthesis. Precamb. Res. 2008, 160, 179–210.
- [7] Fritz, H.; Abdelsalam, M.; Ali, K.A.; Bingen, B.; Collins, A.; Fowler, A.R.; Ghebrab, W.; Hauzenberger, C.A.; Johnson, P.; Kusky, T.; Macey, P.; Muhongo, S.; Stern, R.J.; Viola, G. Orogen styles in the East African Orogens: A review of Neoproterozoic to early Phanerozoic tectonic evolution. J. Afr. Earth Sci. 2013, 86, 65–106.
- [8] Abu Alam, T.S.; Santosh, M.; Brown, M.; and Stüwe, K. Gondwana collision. Mineral. and Petrol. 2013, 107, 631–634.
- [9] Abu Alam, T.S.; Hassan, M.; Stüwe, K.; Meyer, S.; Passchier, C. Multistage tectonism during Gondwana Collision: Baladiyah Complex, Saudi Arabia. J. Petrol. 2014, 55, 1941–1964.
- [10] Blades, M.L.; Collins, A.S.; Foden, J.; Payne, J.L.; Xu, X.; Alemu, T.; Woldetinsae, G.; Clark, C.; Taylor, R. J.M. Age and hafnium isotopic evolution of the Didesa and Kemashi Domains, western Ethiopia. Precamb. Res. 2015, 270, 267–284.
- [11] Stern, R.J. Crustal evolution in the East African Orogen: a neodymium isotopic perspective. J. Afr. Earth Sci. 2002, 34, 109–117.
- [12] Moghazi, A.M. Geochemistry and petrogenesis of a high-K calc-alkaline Dokhan volcanic suite, South Safaga area, Egypt: the role of late Neoproterozoic crustal extension. Precamb. Res. 2003, 423, 161–178.
- [13] Meert, J.G. A synopsis of events related to the assembly of eastern Gondwana. Tectonophysics 2003, 362, 1–40.
- [14] Stoeser, D.B.; Frost, C.D. Nd, Pb, Sr, and O isotopic characterization of Saudi Arabian Shield terranes. Chem. Geol. 2006, 226, 163–188.
- [15] Ali, K.A.; Azer, M.K.; Gahlan, H.A.; Wilde, S.A.; Samuel, M.D.; Stern, R.J. Age constraints on the formation and emplacement of Neoproterozoic ophiolites along the Allaqui-Heiani Suture, South Eastern Desert of Egypt. Gondwana Res. 2010, 18, 583–595.
- [16] Eyal, M.; Litvinovsky, B.; Jahn, B.M.; Zavilevich, A.; Katzir, Y. Origin and evolution of post-collisional magmatism: Coeval Neoproterozoic calc-alkaline and alkaline suites of the Sinai Peninsula. Chem. Geol. 2010, 269, 153–179.
- [17] Be'eri-Shlevin, Y.; Samuel, M.D.; Azer, M.K.; Ramo, O.T.; Whitehouse, M.J.; Moussa, H.E. The Ediacaran Ferani and Rutig volcano-sedimentary successions of the northernmost Arabian-Nubian Shield (ANS): New insights from zircon U-Pb geochronology, geochemistry, and O-Nd isotope ratios. Precamb. Res. 2011, 188, 21–44.
- [18] Hussein, A.A.; Ali, M.M.; El Ramly, M.F. A proposed new classification of the granites of Egypt. J. Volcanol. Geoth. Res. 1982, 14, 187 – 198.
- [19] Bentor, Y.K. The crustal evolution of the Arabo-Nubian Massif with special reference to the Sinai Peninsula. Precamb. Res. 1985, 28, 1–74.
- [20] Hassan, M.A.; Hashad, A.H. Precambrian of Egypt. In: Said R, ed. The geology of Egypt. Balkema, Rotterdam, 1990, p. 201–248.
- [21] Johnson, P.R.; Woldehaimanot, B. Development of the Arabian-Nubian Shield. Perspectives on accretion and deformation in the northern East African Orogen and the assembly of Gondwana. J. Geol. Soc. London, Special Publ. 2003, 206, 290–325.
- [22] Stein, M. Tracing the plume material in the Arabian-Nubian Shield. Precamb. Res. 2003, 123, 223–234.
- [23] Robinson, F.A.; Foden, J.D.; Collins, A.S.; Payne, J.L. Arabian Shield magmatic cycles and their relationship with Gondwana assembly: Insights from zircon U-Pb and Hf isotopes. Earth Planet. Sci. Lett. 2014, 408, 207–225.
- [24] Pease, V.; Yeshanew, F. G.; Whitehouse, M.J. Deciphering crustal growth in the southernmost Arabian Shield through zircon U-Pb geochronology, whole rock chemistry and Nd isotopes, Inter. Geol. Rev. 2022, 64, 2359–2377.
- [25] Be'eri-Shlevin, Y.; Katzir, Y.; Blichert-Toft, J.; Kleinhanns, I.C.; Whitehouse, M. J. Nd-Sr-Hf-O isotope provinciality in the northernmost Arabian-Nubian Shield: implications for crustal evolution. Contrib. Mineral. Petrol. 2010, 160, 181–201.
- [26] Yeshanew, F.G.; Pease, V.; Whitehouse, M.J.; Al-Khirbashi, S. Zircon U-Pb geochronology and Nd isotope systematics of the Abas terrane, Yemen: Implications for Neoproterozoic crust reworking events. Precamb. Res. 2015, 267, 106–120.
- [27] Ghoneim, M.F.; Bjørlykke, A.; Harraz, H.Z. Rb/Sr and Sm/Nd Isotopic Systems of El Sukari Granite, Eastern Desert, Egypt. Proc. 1st Inter. Conf. Geol. Africa, Assiut, Egypt 1999, I, 281–282.
- [28] Dawood, Y.H.; Saleh, G.M.; Abd EL-Naby, H.H. Effects of Hydrothermal Alteration on Geochemical Characteristics of the El Sukari Granite, Central Eastern Desert, Egypt. Inter. Geol. Rev. 2005, 47, 1316–1329.
- [29] Mohamed, H.A.; Ali, S.; Sedki, T.; Abdel Khalik, I. The Sukari Neoproterozoic granitoids, Eastern Desert, Egypt: Petrological and structural implications. J. Afr. Earth Sci. 2019, 149, 426–440.
- [30] Lundmark, A. M.; Andresen, A.; Hassan, M. A.; Augland, L. E.; and Boghdady, G. Y. Repeated magmatic pulses in the East African Orogen in the Eastern Desert, Egypt: an old idea supported by new evidence. Gondwana Res. 2012, 22, 227–237.

- [31] Talavera, C. Zircon SHRIMP geochronology of samples from Sukkari Porphyry (Egypt). Unpubl. Rep. Greg Hall, 2013, p. 12.
- [32] Zoheir, B.; Holzheid, A.; Zeh, A.; McAleer, R.; El-Behairy, M.; Schwarz-Schampera, U.; Lentz, D.; Xiong, F. The Sukari Gold Deposit, Egypt: Geochemical and Geochronological Constraints on the Ore Genesis and Implications for Regional Exploration. *Econ. Geol.* 2023, 118, 719–744.
- [33] Arslan, A.I. Contribution to the Geochemistry of the El Sukari Granite Pluton, Eastern Desert, Egypt. Proc. 1st Conf. Geochem., Alexandria University, Egypt 1989, I, p. 1–18.
- [34] Sharara, N.; Vennemann, T. W. Composition and origin of the fluid responsible for gold mineralization in some occurrences in the Eastern Desert, Egypt: Evidence from fluid inclusions and stable isotopes: Proc. 1st Inter. Conf. Geol. Africa, Assiut, Egypt 1999, I, p. 421–445.
- [35] Sharara, N. Stable isotopes and fluid inclusions of the gold mineralization in El Sukari district, central Eastern Desert: Genetic constraints: Proc. 4th Conf. Geochem., Alexandria University, Egypt 1999, I, p. 317–339.
- [36] Helmy, H.; Kaindl, R.; Fritz, H.; Loizenbauer, J. The Sukari Gold Mine, Eastern Desert, Egypt: structural setting, mineralogy, and fluid inclusion study. *Mineral. Deposita* 2004, 39, 495–511.
- [37] El Sharkawy, M.A.; El-Bayoumi, R. The ophiolites of Wadi Ghadir area, Eastern Desert, Egypt. *Ann. Geol. Surv. Egypt* 1979, 9, 125–135.
- [38] Harraz, H.Z. Lithochemical Prospecting and Genesis of Gold Deposit in the El Sukari Gold Mine, Eastern Desert, Egypt. Unpubl. Ph.D. thesis, Tanta Univ., Egypt 1991, p. 494.
- [39] El Beheiry, M.H.A. Structural Investigation of Thrust System Controlling Gold Mineralization in Sukari Mine Area, Central Eastern Desert, Egypt. Unpubl. M.Sc. Thesis, Tanta Univ., Egypt 2016, p. 245.
- [40] Abd El-Wahed, M.A.; Harraz, H.; El-Behairy, M.H. Transpressional imbricate thrust zones controlling gold mineralization in the Central Eastern Desert of Egypt. *Ore Geol. Rev.* 2016, 78, 424–446.
- [41] Vail, J. R. Pan African crustal accretion in northeast Africa. *J. Afr. Earth Sci.* 1983, 1, 285–294.
- [42] El Gaby, S.; List, F.K.; Tehrani, R. The basement complex of the Eastern Desert and Sinai. In: Said R, ed. *The geology of Egypt*. Balkema, Rotterdam, 1990, p. 75–184.
- [43] Cavaney, R.J. Geology of Sukari Gold Mine, Eastern Desert, Egypt. Unpubl. Internal Rep., Centamin Egypt Ltd and Pharaoh Gold Mines 2005.
- [44] Scoates, J.S.; Wall, C. J. Geochronology of layered intrusions. In: Charlier B et al, eds. *Layered Intrusions*. Dordrecht: Springer, 2015, p. 3–74.
- [45] Wiedenbeck, M.; Allé, P.; Corfu, F.; Griffin, W.L.; Meier, M.; Oberli, F.; Quadt, A.V.; Roddick, J.C.; and Spiegel, W. Three natural zircon standards for U-Th-Pb, Lu-Hf, trace element and REE analyses. *Geostand. Newslett.* 1995, 19, 1–23.
- [46] Black, L.P.; Kamo, S.L.; Allen, C.M.; Davis, D.W.; Aleinikoff, J.N.; Valley, J.W.; Mundil, R.; Campbell, I.H.; Korsch, R.J.; Williams, I.S.; Foudoulis, C. Improved $^{206}\text{Pb}/^{238}\text{U}$ microprobe geochronology by the monitoring of a trace-element-related matrix effect; SHRIMP, ID-TIMS, ELA-ICP-MS and oxygen isotope documentation for a series of zircon standards. *Chem. Geol.* 2004, 205, 115–140.
- [47] Sláma, J.; Kostler, J.; Condon, D. J.; Crowley, J. L.; Gerdes, A.; Hanchar, J. M.; Turbett, M. N. Plešovice—a new natural reference material for U-Pb and Hf isotopic analysis. *Chem. Geol.* 2008, 249, 1–35.
- [48] Ludwig, K.R. SQUID 1.02: a user's manual. Berkeley Geochronology Centre, Special Publ. Berkeley 2001, p. 19.
- [49] Godet, A.; Guilmette, C.; Labrousse, L.; Smit, M.A.; Cutts, J.A.; Davis, D.W.; Vanier, M.A. Lu-Hf garnet dating and the timing of collisions: Palaeoproterozoic accretionary tectonics revealed in the Southeastern Churchill Province, Trans-Hudson Orogen, Canada. *J. Meta. Geol.* 2021, 39, 12599.
- [50] Blichert-Toft, J.; Boyet, M.; Telouk, P.; Albarede, F. ^{147}Sm - ^{143}Nd and ^{176}Lu - ^{176}Hf in eucrites and the differentiation of the HED parent body. *Earth Planet. Sci. Lett.* 2002, 204, 167–181.
- [51] Vervoort, J. D.; Patchett, P. J.; Söderlund, U.; Baker, M. Isotopic composition of Yb and the determination of Lu concentrations and Lu/Hf ratios by isotope dilution using MC-ICPMS. *Geochem. Geophys. Geosyst.* 2004, 5, 1–15.
- [52] Söderlund, U.; Patchett, P. J.; Vervoort, J. D.; Isachsen, C. E. The ^{176}Lu decay constant determined by Lu-Hf and U-Pb isotope systematics of Precambrian mafic intrusions. *Earth Planet. Sci. Lett.* 2004, 219, 311–324.
- [53] Blichert-Toft, J.; Albarède, F. The Lu-Hf isotope geochemistry of chondrites and the evolution of the mantle-crust system. *Earth Planet. Sci. Lett.* 1997, 148, 243–258.
- [54] Vervoort, J. D.; Blichert-Toft, J. Evolution of the depleted mantle: Hf isotope evidence from juvenile rocks through time. *Geochim. Cosmochim. Acta* 1999, 63, 533–556.
- [55] Griffin, W.L.; Wang, X.; Jackson, S.E.; Pearson, N.J.; O'Reilly, S.Y.; Xu, X.; Zhou, X. Zircons chemistry and magma genesis in SE China: in situ analysis of Hf isotopes, Pingtan and Tonglu igneous complexes. *Lithos* 2002, 61, 237–269.
- [56] Belousova, E.A.; Kostitsyn, Y.A.; Griffin, W.L.; Begg, G.C.; O'Reilly, S.Y.; Pearson, N.J. The growth of the continental crust: Constraints from zircon Hf-isotope data. *Lithos* 2010, 119, 457–466.
- [57] Streckeisen A.; Le Matire R.W. A chemical approximation to the modal QAPF classification of igneous rocks. *Neues Jahrb. Mineral. Abh.* 1979, 136, 169–206.
- [58] O'Connor, J.T. A classification for quartz rich igneous rocks based on feldspar ratios. *US Geol. Surv. Prof. Pap.* 1965, B525, USGS, 79–84.

- [59] Sun, S.S.; McDonough W.F. Chemical and isotopic systematics of oceanic basalts: implications for mantle composition and processes. In: Saunders AD, Norry MJ (eds) Magmatism in ocean basins. *J. Geol. Soc. London* 1989, 42, 313–345.
- [60] Pearce, J.A. Trace element characteristics of lavas from destructive plate boundaries. In: Thorpe RS, ed. *Andesites*, John Wiley and Sons 1982, p. 525–548.
- [61] McCulloch, M.T.; Gamble, J.A. Geochemical and geodynamical constraints on subduction zone magmatism. *Earth Planet. Sci. Lett.* 1991, 102, 358–374.
- [62] Whalen, J.B.; Jenner, G.A.; Longstaffe, F.J.; Robert, F.; Gariepy, C. Geochemical and Isotopic (O, Nd, Pb and Sr) Constraints on A-type Granite Petrogenesis Based on the Topsails Igneous Suite, Newfoundland Appalachians. *J. Petrol.* 1996, 37, 1463–1489.
- [63] Shand, S.J. Eruptive rocks. Their genesis, composition, classification, and their relation to ore deposits with a chapter on meteorite. New York: John Wiley and Sons 1943.
- [64] Maniar P.D.; Piccoli P.M. Tectonic discrimination of granitoids. *Geol. Soc. Am. Bull.* 1989, 101, 635–643.
- [65] Frost, B.R.; Barnes, C.G.; Collins, W.J.; Arculus, R.J.; Ellis, D.J.; Frost, C.D. A geochemical classification for granitic rocks. *J. Petrol.* 2001, 42, 2033–2048.
- [66] Pearce J.A.; Harris N.B.W.; Tindle A.G. Trace element discrimination diagrams for the tectonic interpretation of granitic rocks. *J. Petrol.* 1984, 25, 959–983.
- [67] Förster, H.-J.; Tischendorf, G.; Trumbull, R.B. An evaluation of the Rb vs. (Y + Nb) discrimination diagram to infer tectonic setting of silicic igneous rocks. *Lithos* 1997, 40, 261–293.
- [68] Christiansen, E.H.; Keith, J.D. Trace element systematics in silicic magmas: A metallogenetic perspective: Geological Association of Canada Short Course Notes, Trace Element Geochemistry of Volcanic Rocks, Winnipeg, Manitoba Canada 1996, 12, p. 115–151.
- [69] Harris N.B.; Pearce J.A.; Tindle A.G. Geochemical characteristics of collision-zone magmatism. *J. Geol. Soc. London* 1986, 19, 67–81.
- [70] Corfu, F.; Hanchar, J.M.; Hoskin, P.W.O.; Kinny, P. Atlas of zircon textures. A review. *Mineral. Geochem.* 2003, 53, 469–500.
- [71] Hoskin, P.W.O.; Ireland, T.R. Rare earth element chemistry of zircon and its use as a provenance indicator. *Geology* 2000, 28, 627–630.
- [72] Belousova, E.A.; Griffin, W.L.; O'Reilly, S.Y.; Fisher, N.I.I. Igneous zircon: trace element composition as an indicator of source rock type. *Contrib. Mineral. Petrol.* 2002, 143, 602–622.
- [73] Gehrels, G.E.; Valencia, V.; Ruiz, J. Enhanced precision, accuracy, efficiency, and spatial resolution of U-Pb ages by laser ablation-multicollector-inductively coupled plasma-mass spectrometry. *Geochem. Geophys. Geosyst.* 2008, 9, Q03017.
- [74] Spencer, C.J.; Kirkland, C.L.; Taylor, R.J.M. Strategies towards statistically robust interpretations of in situ U-Pb zircon geochronology. *Geosci. Front.* 2016, 7, 581–589.
- [75] Ali, K.A.; Moghazi, A.-K.-M.; Maurice, A.E.; Omar, S.A.; Wang, Q.; Wilde, S.A.; Moussa, E. M.; Manton, W.I.; Stern, R.J. Composition, age, and origin of the ~ 620 Ma Humr Akarim and Humrat Mukbid A-type granites: no evidence for pre-Neoproterozoic basement in the Eastern Desert, Egypt. *Inter. J. Earth Sci.* 2012, 101, 1705–1722.
- [76] Ali, K.A.; Simon, W.A.; Stern, R.J.; Moghazi, A.-K.M.; Mahbubul Ameen, S.M. Hf isotopic composition of single zircons from Neoproterozoic arc volcanics and post-collision granites, Eastern Desert of Egypt: implications for crustal growth and recycling in the Arabian–Nubian Shield. *Precamb. Res.* 2013, 239, 42–55.
- [77] Weyer, S.; Münker, C.; Rehkämper, M.; Mezger, K., Determination of ultra-low Nb, Ta, Zr and Hf concentrations and the chondritic Zr/Hf and Nb/Ta ratios by isotope dilution analyses with multiple collector ICP-MS. *Chem. Geol.* 2002, 187, 295–313.
- [78] Claiborne, L.L.; Miller, C.F.; Walker, B.A.; Wooden, J.L.; Mazdab, F.K.; Bea, F. Tracking magmatic processes through Zr/Hf ratios in rocks and Hf and Ti zoning in zircons: an example from the Spirit Mountain batholith, Nevada. *Mineral. Mag.* 2006, 70, 517–543.
- [79] Wang, X.; Griffin, W.L.; Chen J. Hf contents and Zr/Hf ratios in granitic zircons. *Geochem. J.* 2010, 44, 65–72.
- [80] El-Bialy, M. Z.; Ali, K. A. Zircon trace element geochemical constraints on the evolution of the Ediacaran (600–614 Ma) post-collisional Dokhan volcanics and younger granites of SE Sinai, NE Arabian-Nubian shield. *Chem. Geol.* 2013, 360–361, 54–73.
- [81] Hinton R.W.; Upton B.G.J. The chemistry of zircon: variations within and between large crystals from syenite and alkali basalt xenoliths, *Geochim. Cosmochim. Acta* 1991, 55, 287–3302.
- [82] Hoskin, P.W.O.; Schaltegger, U. The composition of zircon and igneous and metamorphic petrogenesis. In: Hanchar JM, Hoskin PWO, eds., *Zircon.: Rev. Mineral. Geochem.* 2003, 53, 27–62.
- [83] Hanchar J.M., and van Westrenen W. 2007. Rare earth element behaviour in zircon-melt systems. *Elements* 3, 37–42.
- [84] Nardi, L. V. S.; Formoso, M. L. L.; Jarvis, K.; Oliveira, L.; Neto, A. C. B.; Fontana, E. REE, Y, Nb, U, and Th contents and tetrad effect in zircon from a magmatic–hydrothermal F-rich system of Sn-rare metalcryolite mineralized granites from the Pitinga Mine, Amazonia, Brazil. *J. South Am. Earth Sci.* 2012, 33, 34–42.
- [85] Hoskin, P.W.O. Trace-element composition of hydrothermal zircon and the alteration of Hadean zircon from the Jack Hills, Australia. *Geochim. Cosmochim. Acta* 2005, 69, 637–648.

- [86] Hoskin, P.W.O.; Kinny, P.D.; Wyborn, D.; Chappell, B.W. Identifying accessory mineral saturation during differentiation in granitoid magmas: an integrated approach. *J. Petrol.* 2000, 41, 1365–1396.
- [87] Claiborne, L. L.; Miller, C.; Wooden, J. Trace element composition of igneous zircon: A thermal and compositional record of the accumulation and evolution of a large silicic batholith, Spirit Mountain, Nevada. *Contrib. Mineral. Petrol.* 2010, 160, 511–531.
- [88] Claiborne, L. L.; Wooden, J. L.; Miller, C. F.; Gualda, G. A.; Clyne, M. A.; Flanagan, D. M. Understanding the Mount St. Helens magmatic system using zircon surface geochronology and geochemistry, 3d x-ray tomography, and glass compositions. *Geol. Soc. Am. Abs. with Programs* 2012, 44, p. 74.
- [89] Yao, J.; Shu, L.; Santosh, M.; Li, J. Precambrian crustal evolution of the South China Block and its relation to supercontinent history: Constraints from U–Pb ages, Lu–Hf isotopes and REE geochemistry of zircons from sandstones and granodiorite. *Precamb. Res.* 2012, 208–211, 19–48.
- [90] Barth, A. P.; Wooden, J. L. Coupled elemental and isotopic analyses of polygenetic zircons from granitic rocks by ion microprobe, with implications for melt evolution and the sources of granitic magmas. *Chem. Geol.* 2010, 277, 149–159.
- [91] Belousova, E.A.; Griffin, W.L.; O'Reilly, S.Y. Zircon morphology, trace element signatures and Hf-isotope composition as a tool for petrogenetic modelling: examples from Eastern Australian granitoids. *J. Petrol.* 2006, 47, 329–353.
- [92] Orejana, D.; Villaseca, C.; Valverde-Vaquero, P.; Belousova, E.A.; Armstrong, R.A. U–Pb geochronology and zircon composition of late Variscan S- and I-type granitoids from the Spanish Central System batholith. *Inter. J. Earth Sci.* 2012, 101, 1789–1815.
- [93] Wang, Q.; Zhu, D. C.; Zhao, Z. D.; Guan, Q.; Zhang, X. Q.; Sui, Q. L.; Moa, X. X. Magmatic zircons from I-, S- and A-type granitoids in Tibet: Trace element characteristics and their application to detrital zircon provenance study. *J. Asian Earth Sci.* 2012, 53, 59–66.
- [94] Harrison, T. M.; Watson, E. B.; Aikman, A. B. Temperature Spectra of Zircon Crystallization in Plutonic Rocks. *Geology* 2007, 35, 635–638.
- [95] Page, L.; Hermansson, T.; Söderlund, P.; Stephens, M. B. $^{40}\text{Ar}/^{39}\text{Ar}$ and U–Th/He geochronology: Phase 2. Forsmark site investigation, 2007, SKB P-06-211, Svensk Kärnbränslehantering AB.
- [96] Fu, B.; Page, F.Z.; Cavosie, A.J.; Clechenko, C.C.; Fournelle, J.; Kita, N.T.; Lackey, J.S.; Wilde, S.A.; Valley, J.W. Ti-in-zircon thermometry: applications and limitations. *Contrib. Mineral. Petrol.* 2008, 156, 197–215.
- [97] Kaczmarek, M.-A.; Müntener, O.; Rubatto, D. Trace element chemistry and U–Pb dating of zircons from oceanic gabbros and their relationship with whole rock composition (Lanzo, Italian Alps). *Contrib. Mineral. Petrol.* 2008, 155, 295–312.
- [98] Cates, N. L.; Mojzsis, S. J. Metamorphic zircon, trace elements and Neoarchean metamorphism in the ca. 3.75 Ga Nuvvuagittuq supracrustal belt, Quebec (Canada). *Chem. Geol.* 2009, 261, 98–113.
- [99] Ickert, R.B.; Williams, I.S.; Wyborn, D. Ti in zircon from the Boggy Plain zoned pluton: implications for zircon petrology and Hadean tectonics. *Contrib. Mineral. Petrol.* 2011, 162, 447–461.
- [100] Orejana, D.; Villaseca, C.; Armstrong, R.A.; Jeffries, T.E. Geochronology and trace element chemistry of zircon and garnet from granulite xenoliths: constraints on the tectonothermal evolution of the lower crust under central Spain. *Lithos* 2011, 124, 103–116.
- [101] Wang, F.; Liu, S. A.; Li, S.; He, Y. Contrasting zircon Hf–O isotopes and trace elements between ore-bearing and ore-barren adakitic rocks in central-eastern China: Implications for genetic relation to Cu–Au mineralization. *Lithos* 2013, 156–159, 97–111.
- [102] Feteha, B.F.; Lentz, D.R.; El Bouseily, A.M.; Khalil, K.I.; Khamis, H.A.; Moghazi, A-K.M. Petrogenesis of Neoproterozoic Mo-bearing A-type granites in the Gattar area, northern Eastern Desert, Egypt: implications for magmatic evolution and mineralization processes. *Ore Geol. Rev.* 2022, 148, 105007.
- [103] Watson, E.B.; Harrison, T.M. Zircon thermometer reveals minimum melting conditions on earliest Earth. *Science* 2005, 308, 841–844.
- [104] Watson, E.B.; Wark, D.A.; Thomas, J.B. Crystallization thermometers for zircon and rutile. *Contrib. Mineral. Petrol.* 2006, 151, 413–433.
- [105] Ferry, J.M.; Watson, E.B. New thermodynamic models and revised calibrations for the Ti-in-zircon and Zr-in-rutile thermometers. *Contrib. Mineral. Petrol.* 2007, 154, 429–437.
- [106] Ghiorso, M.S.; Gualda, G.A.R. A method for estimating the activity of titania in magmatic liquids from the compositions of coexisting rhombohedral and cubic iron titanium oxides: *Contrib. Mineral. Petrol.* 2013, 165, 73–81.
- [107] Zhang, X.; Lentz, D.R.; Yao, C.L.; Liu, R.; Yang, Z.; Mei, Y.X.; Fan, X.W.; Huang, F.; Qin, Y.; Zhang, K.; Zhang, Z.F. Geochronology, geochemistry, and Sr–Nd–Pb–Hf isotopes of the Zhunsijihua granitoid intrusions associated with the molybdenum deposit, northern Inner Mongolia, China: implications for petrogenesis and tectonic setting. *Inter. J. Earth Sci.* 2018, 107, 687–710.
- [108] Zhang, X.; Chai, F.; Chen, C.; Quan, H.; Wang, K.; Li, S.; Wu, S. Using whole rock and zircon geochemistry to assess porphyry copper potential of the Tonggou Copper Deposit, Eastern Tianshan. *Minerals* 2020, 10, 10070584.
- [109] Cates, N. L.; Mojzsis, S. J. Metamorphic zircon, trace elements and Neoarchean metamorphism in the

- ca. 3.75 Ga Nuvvuagittuq supracrustal belt, Quebec (Canada). *Chem. Geol.* 2009, 261, 98–113.
- [110] Pearce, J.A.; Peate, D.W. Tectonic implications of the composition of volcanic arc magmas: *Ann. Rev. Earth Planet. Sci.* 1995, 23, 251–285.
- [111] Gao, L. E.; Zeng, L. S.; Hu, G. Y.; Wang, Y. Y.; Wang, Q.; Guo, C. L.; Hou, K. Early Paleozoic magmatism along the northern margin of East Gondwana. *Lithos* 2019, 334–335, 25–41.
- [112] Saalfeld, M.A.; Kelley, D.F.; Pantera, K.S. Insight on magma evolution and storage through the recent eruptive history of Cotopaxi Volcano, Ecuador. *J. South Am. Earth Sci.* 2019, 93, 85–101.
- [113] Schiano, P.; Monzier, M.; Eissen, J.-P.; Martin, H.; Koga, K. T. Simple mixing as the major control of the evolution of volcanic suites in the Ecuadorian Andes. *Contrib. Mineral. Petrol.* 2010, 160, 297–312.
- [114] Wang, X.-C.; Wilde, S.A.; Li, Z.-X.; Li, S.; Li, L. Do Supercontinent-Superplume Cycles Control the Growth and Evolution of Continental Crust? *J. Earth Sci.* 2020, 31, 1142–1169. <https://doi.org/10.1007/s12583-020-1077-4>
- [115] Bacon, C.R.; Druitt, T.H. Compositional evolution of the zoned calc-alkaline magma chamber of Mount Mazama, Crater Lake, Oregon. *Contrib. Mineral. Petrol.* 1988, 118, 111–129.
- [116] Guffanti, M.; Clyne, M.A.; Muffler, L.J.P. Thermal and mass implications of magmatic evolution in the Lassen volcanic region, California, and constraints on basalt influx to the lower crust. *J. Geophys. Res.* 1996, 101, 3001–3013.
- [117] Petford, N.; Atherton, M.P. Na-rich partial melts from newly underplated basaltic crust: The Cordillera Blanca Batholith, Peru. *J. Petrol.* 1996, 37, 1491–1521.
- [118] Martin, H.; Smithies, R.H.; Rapp, R.; Moyen, J.F.; Champion, D. An overview of adakite, tonalite–trondhjemite–granodiorite (TTG), and sanukitoid: relationships and some implications for crustal evolution. *Lithos* 2005, 79, 1–24.
- [119] Laurent, O.; Martin, H.; Moyen, J.F.; Doucelance, R. The diversity and evolution of late-Archean granitoids: evidence for the onset of “modern-style” plate tectonics between 3.0 and 2.5 Ga. *Lithos* 2014, 196–197, 131–149.
- [120] Bergemann, C.; Jung, S.; Berndt, J.; Stracke, A.; Hauff, F. Generation of magnesian, high-K alkali-calcic granites and granodiorites from amphibolitic continental crust in the Damara orogen, Namibia. *Lithos* 2014, 198–199, 217–233.
- [121] Manya, S.; Maboko, M.A.H. Generation of Palaeoproterozoic tonalites and associated high-K granites in southwestern Tanzania by partial melting of underplated mafic crust in an intracontinental setting: Constraints from geochemical and isotopic data. *Lithos* 2016, 260, 120–133.
- [122] Simon, I.; Jung, S.; Romer, R.L.; Garbe-Schönberg, D.; Berndt, J. Geochemical and Nd-Sr-Pb isotope characteristics of synorogenic lower crust-derived granodiorites (Central Damara orogen, Namibia). *Lithos* 2017, 274–275, 397–411.
- [123] Arth, J.G.; Baker, F.; Peterman, Z.E.; Friedman, I. Geochemistry of the gabbro-diorite-tonalite-trondhjemite suite of southwest Finland and its implications for the origin of tonalite and trondhjemite magmas. *J. Petrol.* 1978, 19, 289–316.
- [124] Shellnutt, J.G.; Wang, C.Y.; Zhou, M-F.; Yang, Y. Zircon Lu-Hf isotopic compositions of metaluminous and peralkaline A-type granitic plutons of the Emeishan large igneous province (SW China): Constraints on the mantle source. *J. Asian Earth Sci.* 2009, 35, 45–55.
- [125] Hofmann, A.W.; White, W.M. Ba, Rb and Cs in the Earth’s Mantle. *Zeitschrift fur Naturforschung A. J. Phys. Sci.* 1983, 38, 256–266.
- [126] Rudnick, R.L.; Fountain, D.M. Nature and composition of the continental crust: a lower crustal perspective. *Rev. Geophy.* 1995, 33: 267–309.
- [127] Defant, M. J.; Drummond, M. S. Derivation of some modern arc magmas by melting of young subducted lithosphere. *Nature* 1990, 347, 662–665.
- [128] Martin, H. Adakitic Magmas: Modern Analogues of Archaean Granitoids. *Lithos*, 1999, 46, 411–429.
- [129] Wang, X.-C.; Li, X.-H.; Li, W.-X.; Li, Z.-X. Ca-825 Ma komatiitic basalts in South China: First evidence for 1500 °C mantle melts by a Rodinian mantle plume. *Geology* 2007, 35, 1103.
- [130] Zoheir, B.; El-Bialy, M.; Ragab, A.; Deshesh, F.; Zeh, A.; Steele-MacInnis, M. Hybrid granite magmatism during orogenic collapse in the Eastern Desert of Egypt: Inferences from whole-rock geochemistry and zircon U-Pb–Hf isotopes. *Precamb. Res.* 2021, 354, 106044.
- [131] Be’eri-Shlevin, Y.; Katzir, Y.; Blichert-Toft, J.; Kleinhanns, I.C.; Whitehouse, M. J. Nd–Sr–Hf–O isotope provinciality in the northernmost Arabian–Nubian Shield: implications for crustal evolution. *Contrib. Mineral. Petrol.* 2010, 160, 181–201.
- [132] Kemp, A. I. S.; Hawkesworth, C. J.; Paterson, B. A.; Kinny, P. D. Episodic growth of the Gondwana supercontinent from hafnium and oxygen isotopes in zircon. *Nature* 2006, 439, 580–583. doi:10.1038/nature04505.
- [133] Hargrove, U.S.; Stern, R.J.; Kimura, J.I.; Manton, W.I.; Johnson, P.R. How juvenile is the Arabian–Nubian Shield? Evidence from Nd isotopes and pre-Neoproterozoic inherited zircon in the Bi’r Umq suture zone, Saudi Arabia: *Earth Planet. Sci. Lett.* 2006, 252, 308–326.